

**REFURBISHING A SCANNING TRANSMISSION ELECTRON MICROSCOPE**

By

Daniel J. Ballard

A thesis submitted in partial fulfillment of the requirements for  
the degree of

Bachelor of Science

Houghton College

December 2014

Signature of Author \_\_\_\_\_

Department of Physics  
December 13, 2014

\_\_\_\_\_  
Dr. Brandon Hoffman  
Associate Professor of Physics  
Research Supervisor

\_\_\_\_\_  
Dr. Mark Yuly  
Professor of Physics

# REFURBISHING A SCANNING TRANSMISSION ELECTRON MICROSCOPE

By

Daniel J. Ballard

Submitted to the Houghton College Department of Physics  
on December 13, 2014 in partial fulfillment of the requirement for  
the degree of Bachelor of Science

## **Abstract**

A Jeol 100CX scanning transmission electron microscope (STEM) is being rehabilitated with the intention of using it to explore microstructures of thin metal films. The vacuum system has been analyzed and tested. Modification of the electronics has allowed for more efficient troubleshooting techniques.

Thesis Supervisor: Dr. Brandon Hoffman

Title: Associate Professor of Physics

## TABLE OF CONTENTS

<b>Chapter 1 HISTORY AND MOTIVATION</b> .....	<b>8</b>
<b>1.1 Introduction</b> .....	<b>8</b>
<b>1.2 Development of the Transmission Electron Microscope (TEM)</b> .....	<b>8</b>
1.2.1 Wave-like Properties of Electrons.....	8
1.2.2 The First TEM – Knoll and Ruska.....	10
1.2.3 Further Developments and Commercial Production.....	12
<b>1.3 Density Contrast</b> .....	<b>13</b>
<b>1.4 Electron Diffraction</b> .....	<b>13</b>
1.4.1 Electron Diffraction vs. X-ray Diffraction (XRD).....	13
1.4.2 Selected Area Electron Diffraction (SAED or SAD).....	15
1.4.3 Convergent Beam Electron Diffraction (CBED).....	16
<b>1.5 History the JEOL 100CX TEM at Houghton College</b> .....	<b>16</b>
<b>Chapter 2 THEORY</b> .....	<b>17</b>
<b>2.1 Introduction</b> .....	<b>17</b>
<b>2.2 Wave/Particle Duality</b> .....	<b>17</b>
2.2.1 Relating Electron Energy to Wavelength.....	17
2.2.2 Relating Wavelength to Resolving Power.....	19
<b>2.3 Electron/Matter Interaction</b> .....	<b>22</b>
2.3.1 Scattering as Particles.....	23
2.3.2 Scattering as Waves: Diffraction.....	34
<b>2.4 Imaging and Analysis Techniques based on Electron Scattering</b> .....	<b>41</b>
2.4.1 Selected Area Electron Diffraction (SAED).....	42
2.4.2 Convergent Beam Electron Diffraction (CBED).....	45
2.4.3 Scanning Transmission Electron Microscopy (STEM).....	50
2.4.5 Other Characterization Techniques.....	51
<b>2.5 Electron Beam Technology</b> .....	<b>52</b>
2.5.1 Electron Sources.....	52
2.5.2 Electromagnetic Lenses.....	54
2.5.3 Detectors and other Sensors.....	59
2.5.4 Vacuum System.....	63
<b>Chapter 3 ANALYSIS AND MODIFICATION</b> .....	<b>68</b>
<b>3.1 Instrument Overview</b> .....	<b>68</b>
3.1.1 Vacuum System.....	69
3.1.2 Electron Gun.....	73

3.1.3 Optics and Image Formation.....	74
3.1.4 Electronics .....	79
3.1.5 Sensors.....	82
3.1.6 Sample Chamber and Holder .....	88
<b>3.2 Modifications.....</b>	<b>90</b>
3.2.1 Disassembly and Repair of Rotary Vane Pump #2 (RP2) .....	90
3.2.2 Oil Filter Restoration.....	91
3.2.3 Conversion of Valve Control System to Manual Operation.....	91
3.2.4 Disassembly and Cleaning of Diffusion Pumps.....	93
3.2.5 Isolation and Bypass of Desiccator Leak .....	93
<b>Chapter 4 CONCLUSION.....</b>	<b>94</b>
4.1 Summary.....	94
4.2 Future Work.....	95
<b>Appendix A: Modified Systems .....</b>	<b>96</b>
A.1 Manual/Automatic Transfer Switch.....	96
A.2 Molecular Sieve .....	97
<b>Appendix B: Derivation for Relativistic Momentum of an Electron .....</b>	<b>99</b>
<b>Appendix C: Specimen Holders .....</b>	<b>101</b>
C.1 Common specimen holder .....	101
C.2 EM-BST Tilting specimen holder.....	102
C.3 BSR Rotating Holder.....	103
<b>Appendix D: Additional Diagrams and Schematics.....</b>	<b>104</b>

## TABLE OF FIGURES

<i>Figure 1. Bohr model showing the wavelength associated with an electron of a given energy. ....</i>	9
<i>Figure 2. Knoll and Ruska’s first electron microscope design. ....</i>	11
<i>Figure 3. Knoll and Ruska’s ‘supermicroscope’ utilizing a condenser lens before the sample and pole pieces to increase the magnification capability. ....</i>	12
<i>Figure 4. Braggs law. ....</i>	14
<i>Figure 5. When a plane wave is incident on a periodic array of atoms in a specimen, the atoms act as scattering centers for the diffracted waves. ....</i>	14
<i>Figure 6. Optical lens diagram showing <math>\theta</math>, the half-angle of the light cone accepted into the aperture. ....</i>	19
<i>Figure 7. Relativistic and non-relativistic <math>\lambda</math> for electrons with energies from 1 eV to 1 MeV. ....</i>	20
<i>Figure 8. Electrons may be scattered at angles anywhere from 0 to 180 degrees with respect to the incident beam. ...</i>	22
<i>Figure 9. Electron particle scattering due to Coulomb force. ....</i>	23
<i>Figure 10. Geometry of electron scattering. ....</i>	24
<i>Figure 11. An incoming electron can eject an electron from an electron shell of an atom within the sample. ....</i>	29
<i>Figure 12. Bremsstrahlung x-rays given off when an electron is decelerated by coulomb forces from the nucleus of an atom in the specimen. ....</i>	30
<i>Figure 13. Secondary electrons. ....</i>	31
<i>Figure 14. Plasmon oscillation. ....</i>	33
<i>Figure 15. Phonon oscillation. ....</i>	34
<i>Figure 16. Incident waves emanating from a single source are diffracted as they pass through two slits. ....</i>	35
<i>Figure 17. When a plane wave is incident upon a line or plane of scattering centers (atoms, nuclei, electron clouds) the original plane wave is transmitted (called the 0th order). ....</i>	36
<i>Figure 18. The unit cell in at the origin repeats in x, y, and z-directions forming a regular 3-dimensional periodic array of atoms known as a crystal lattice. Taken from ....</i>	37
<i>Figure 19. The lattice plane closest to the origin will pass through the x, y, and z-axes at points that are distances a, b, and c from the origin respectively. ....</i>	38
<i>Figure 20. Examples of Miller indices for three different lattice planes in the same crystal lattice. ....</i>	38
<i>Figure 21. The geometry of the Von Laue scattering model. ....</i>	39
<i>Figure 22. Bragg’s Law. ....</i>	41
<i>Figure 23. Selected area electron diffraction. ....</i>	42
<i>Figure 24. Ray diagrams for SA magnification (left) and SA electron diffraction (right). ....</i>	43
<i>Figure 25. The field limiting (SAD) aperture. ....</i>	44

Figure 26. Different diffraction patterns are formed when a crystal of Al <sub>78</sub> Mn <sub>22</sub> rapidly solidified alloy is tilted 0,18,36, and 54 degrees.....	45
Figure 27. The effect of beam convergence on overlap of diffraction spots in CBED.....	46
Figure 28. Kikuchi line only form when the beam interacts with the hkl diffraction planes over a range of angles. ....	47
Figure 29. Rotational symmetry in the crystal lattice. ....	48
Figure 30. Three examples symmetry in CBED image patterns. ....	48
Figure 31. The scanning convergent beam remains parallel to the optic axis as it scans across the specimen in STEM mode.....	50
Figure 32. Self-biasing Thermionic Emission Electron gun. ....	53
Figure 33. The concentration and strength of the magnetic field increases from (a) to (c). ....	55
Figure 34. Cross section of an Electromagnetic Lens. ....	56
Figure 35. Electromagnetic Lens divided into three force interaction zones.....	57
Figure 36. Cross-products of velocity and B-field vectors by zone.....	57
Figure 37. An electron starting at point P with velocity v will follow a helical trajectory in uniform magnetic field H...	59
Figure 38. Cathodoluminescence occurs when electrons incident on the ZnS screen excite the ZnS and form a luminescent area for a time long enough to be viewed with the human eye or captured on camera. ....	60
Figure 39. Cross section of a semiconductor detector made with layers of Si and Al. ....	61
Figure 40. Classic CCD (left) vs column parallel CCD (right).....	62
Figure 41. Scintillator-photomultiplier tube.....	63
Figure 42. Mechanical Rotary Pump showing inlet, pump chamber, rotor and rotary vanes, ball valve, gas ballast valve, and outlet port.....	65
Figure 43. Rotary vane pumping sequence.....	66
Figure 44. Diffusion Pump attached to the system with a high vacuum flange (5). ....	67
Figure 45. JEOL 100CX main column. ....	68
Figure 46. JEOL 100CX vacuum system. ....	70
Figure 47. A Pirani gauge circuit.....	72
Figure 48. JEOL 100CX self-biasing electron gun.....	73
Figure 49. Optical system of JEOL100CX.....	74
Figure 50. Selected Area (SA) image versus SA diffraction.....	75
Figure 51. Main column cutaway view showing placement of lenses, pole pieces, apertures, and deflection coils.....	76
Figure 52. BF/DF coil unit.....	78
Figure 53. BF/DF coil consists of two sets of solenoid coils. ....	78
Figure 54. High voltage power supply showing HV oscillation circuit (a) and HV rectifying circuit (b).....	80

<i>Figure 55. Lens (a) and deflector coil (b) current stabilization circuits.</i>	80
<i>Figure 56. JEOL 100CX Electrical systems flowchart.</i>	81
<i>Figure 57. The phosphor viewing screen can lay flat, can be tilted 45° for viewing, and can be tilted 90° to allow the electron beam to be transmitted to the camera chamber below.</i>	82
<i>Figure 58. Viewing chamber (A) and camera chamber (C).</i>	84
<i>Figure 59. Open camera chamber.</i>	84
<i>Figure 60. The number of BSEs is affected by surface topography.</i>	85
<i>Figure 61. An electron beam incident on a sample surface (1) of uniform composition will produce a relatively constant number of BSEs.</i>	86
<i>Figure 62. Cross sectional view of ASD system.</i>	87
<i>Figure 63. Effect of tilting a specimen in diffraction mode.</i>	89
<i>Figure 64. X and Y tilt speed control knobs and tilt control pedals.</i>	90
<i>Figure 65. Two-sided vane removed from the rotating drum.</i>	91
<i>Figure 66. Manual valve control schematic.</i>	92
<i>Figure 67 Diagram of the Auto/Manual Mode transfer switch.</i>	97
<i>Figure 68. Common Specimen holder.</i>	101
<i>Figure 69. X-tilt and y-tilt azimuth graph.</i>	102
<i>Figure 70. Compressed air system schematic showing how solenoid valves control air flow to open or close the vacuum system valves.</i>	104

## Chapter 1

### HISTORY AND MOTIVATION

#### 1.1 Introduction

An electron microscope is a tool that can be used to determine the properties of matter on a scale much smaller than that which is observable with the aid of optical microscopes. Optical microscopy allows scientists to probe the nature of matter on a small scale, but the electromagnetic properties of light limit optical microscopes to a scale of about  $10^{-2} - 10^{-6}$ m. Originally developed in 1933 by Knoll and Ruska[1], the electron microscope utilized recent knowledge advances in the field of particle physics to probe matter on a closer and more detailed level. A beam of electrons could be directed and focused in order to both magnify objects and to characterize objects with the use of density contrast and electron diffraction analysis.

#### 1.2 Development of the Transmission Electron Microscope (TEM)

##### 1.2.1 Wave-like Properties of Electrons

In 1925, Louis de Broglie postulated that electrons have wave-like properties.[2] Previous experiments had confirmed that radiation exhibited both wave-like and particle-like behavior. Hertz and Hallwachs (1887) and Phillip Lenard (1900) had demonstrated that metals emit electrons when exposed to electromagnetic waves above a certain frequency (The Photoelectric Effect)[3]. DeBroglie proposed that matter, e.g. electrons, also possessed this wave-particle dual nature.

The most recent atomic model at the time of DeBroglie's research was Bohr's model in which the electrons occupied specific energy levels around the nucleus. Bohr had hypothesized[4] that the angular momentum for an electron in the hydrogen atom is quantized according to

$$pr = \frac{nh}{2\pi} \quad (1)$$

where  $n$  is an integer and  $h$  is Planck's constant. Bohr offered no explanation for why the angular momentum would be quantized.

DeBroglie had an explanation: electrons behaved like waves, and therefore followed standing wave conditions for given energy levels around the nucleus. Mathematically, he proposed[5] the following relations for the frequency  $f$  and wavelength  $\lambda$  of an electron:

$$f = \frac{E}{h} \quad (2)$$

$$\lambda = \frac{h}{p} \quad (3)$$

where  $E$  is the total energy,  $p$  is the momentum,  $h$  is Planck's constant, and  $\lambda$  is called the 'de Broglie wavelength' of the particle.

DeBroglie used his relations to propose an explanation for the quantization of angular momentum in the Bohr model of the Hydrogen atom. He hypothesized that there was a standing wave condition such that the circumference of the orbit of the electron was equivalent to an integer number of wavelengths as seen in Figure 1.

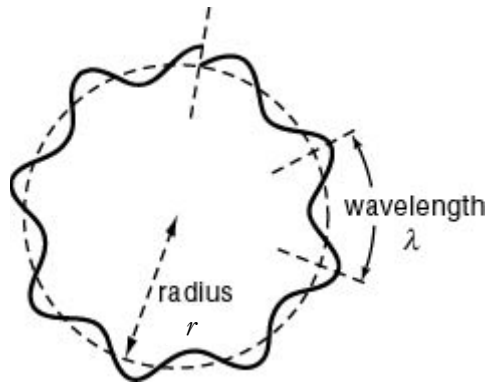


Figure 1. Bohr model showing the wavelength associated with an electron of a given energy. The wavelength in the figure does not meet the standing wave conditions that DeBroglie proposed. A wave that fits the DeBroglie condition would not be broken, but rather follow a continuous path around the circle.

Using Equation (1) and the DeBroglie wavelength of a particle, equation (3), it can be shown that the circumference of the electron's orbit is equal to an integer number of wavelengths.[6]

$$2\pi r = \frac{nh}{p} = n\lambda \quad (4)$$

This hypothesis was experimentally confirmed by two experiments 1927. Davisson and Germer found that electrons exhibited wave-like properties in accordance with DeBroglie's theory by forming an interference pattern as they were scattered from a metal plate.[7] Thomson and Reid accelerated a beam of electrons through ~25kV and they were transmitted through a thin screen area containing a crystal powder. Electrons with this energy, according to DeBroglie's calculations, would have a corresponding wavelength of the order of x-ray beams used in similar diffraction experiments. The results showed that the electron beam produced the same diffraction pattern as the x-ray beam.[8]

### *1.2.2 The First TEM - Knoll and Ruska*

Knoll and Ruska were the first to propose the idea of an electron microscope in a paper published in 1932.[9] Soon afterward they developed the first working electron lenses, and the resolution of the light microscope was surpassed in 1933.

E. Ruska was a graduate student under Max Knoll, head of the Electronics Laboratory at Technical University. Following the discovery by H. Busch in 1927 that the effect of a magnetic coil on an electron beam was analogous to that of a convex lens on an optical beam[10], Ruska devoted his research to the further development of magnetic lenses to be used for focusing electron beams.

Ruska's first design (see Figure 2) consisted of two magnetic lenses—an objective and a projector lens.[11]The magnification of this first microscope was modest, but further developments were quick to follow.

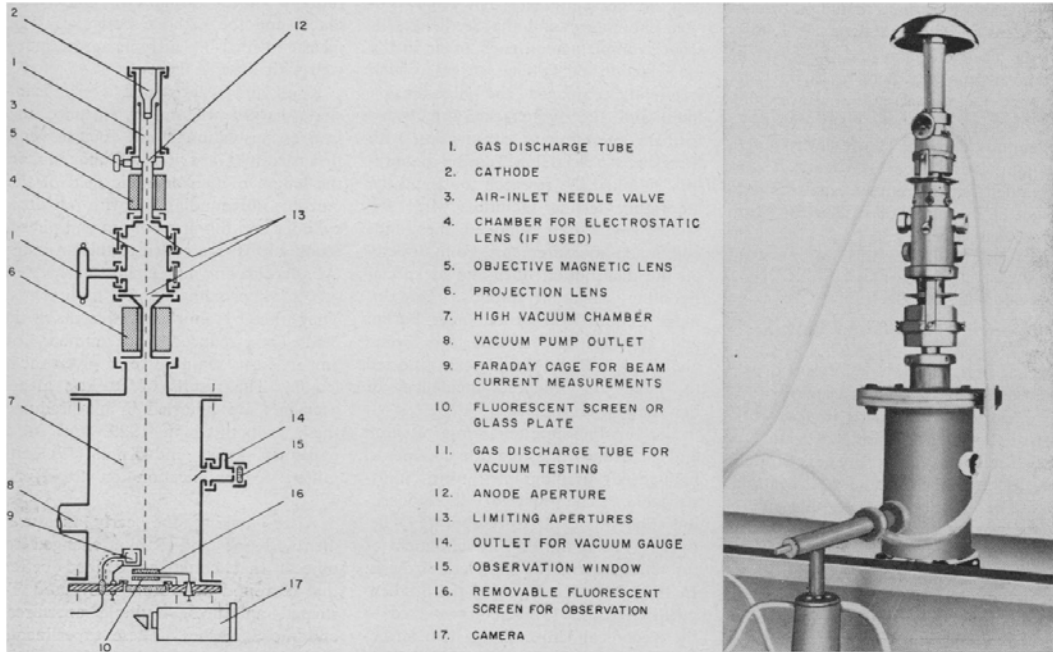


Figure 2. Knoll and Ruska's first electron microscope design. The two EM lenses utilize Ruska's first design with a  $\sim 10\text{mm}$  gap in the iron shrouding. The electron beam passes the object plane, is focused by the first (objective) lens, forming an intermediate image in the image plane of the first lens. This image is then focused again through the second (projector) lens, which will allow for further magnification. Taken from reference [11].

Knoll and Ruska found that electromagnetic lenses could only be practical if the focal length was short enough to build a reasonably sized microscope. Three important discoveries resulted from their research of electromagnetic lenses that enabled the development of the electron microscope. Two of these were improvements in EM lens design, and one was with regard to the arrangement of the lenses in the microscope itself.

First, Ruska discovered that a narrow unshielded gap ( $\sim 10\text{mm}$ ) reduces the number of current coils needed to achieve a given focal length.[12] His first electron microscope featured the narrow unshielded gap design for an electromagnetic lens. Second, Knoll and Ruska found that the addition of a condenser lens between the anode and the object allowed for greater magnification and shorter object distance. The third discovery was that shorter focal lengths can be achieved by narrowing the diameter of the magnetic lenses in addition to having the short gaps.[9]

In 1932, Ruska began working on an improved design for the electron microscope that included interchangeable pole pieces (which effectively narrowed the lens diameter to the electron beam diameter) and a condenser lens as outlined in Figure 3.[11] By 1933, Ruska had produced images of 8000 and 12000 times magnification using this microscope, surpassing the resolution of the optical microscope.[11]

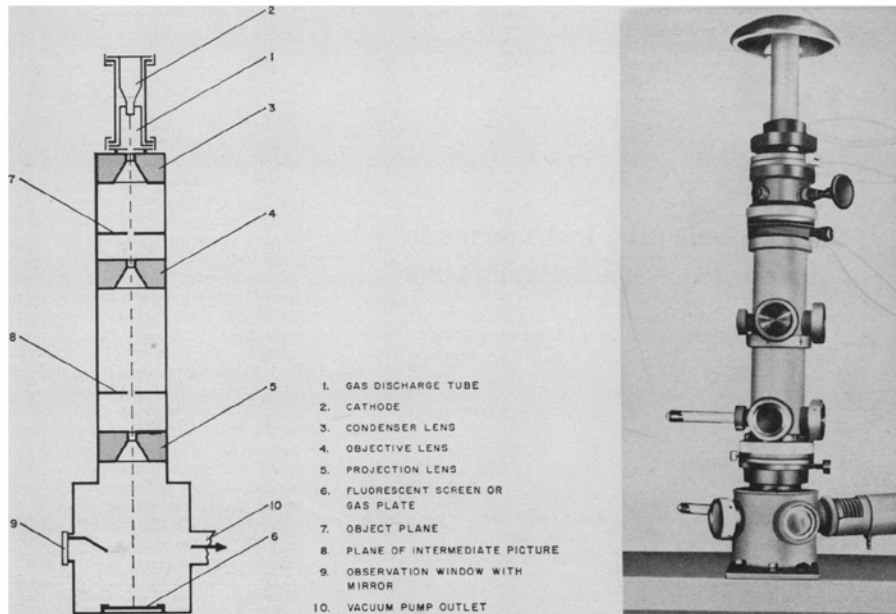


Figure 3. Knoll and Ruska's 'supermicroscope' utilizing a condenser lens before the sample and pole pieces to increase the magnification capability.

### *1.2.3 Further Developments and Commercial Production*

The first commercial Transmission Electron Microscope (TEM) was built in UK in 1936. In 1938, Siemens and Halske, assisted by von Borries and Ruska, developed one that was reliable enough for regular production.[13]

After WWII, TEMs become widely available from many sources, including Hitachi, JEOL, Philips and RCA. The instrument at Houghton College featured in this research project is a JEOL 100CX Scanning Transmission Electron Microscope (STEM). A STEM is a TEM that has been equipped to produce scanning images (a composite image constructed from a matrix of information from discrete points on the sample) as well as regular TEM images containing information from one targeted area.

### 1.3 Density Contrast

During the early years of electron microscope imaging and analysis, the images obtained were density contrast images. The amount of electrons that are scattered or absorbed by a given areas of a sample can vary based on density, structure, or thickness. Density contrast results in the image because some electrons do not reach the viewing screen or imaging medium. A range of intensities can be viewed that corresponds to structural or compositional aspects of the sample.

### 1.4 Electron Diffraction

Electron diffraction analysis, first used in 1927 and developed over the next few decades, was not of immediate importance within TEM analysis. The elektronograf, a similar instrument with beam energies up to 100 keV, was used by B. K. Vainshtein and his colleagues as early as the 1940s.[14]

The concept of analyzing materials using diffraction predates the use of electron diffraction. X-rays were the basis of the Bragg[15] and von Laue[16] models of wave/particle interaction within crystals. Later on, following DeBroglie's theory of the wave/particle dual nature of the electron, Davisson and Germer demonstrated that the same laws that work for x-ray diffraction also work for electron diffraction.

#### *1.4.1 Electron Diffraction vs. X-ray Diffraction (XRD)*

X-ray diffraction (XRD) predates electron diffraction by over a decade, but the basic elements of the diffraction theory apply to both. XRD theory was pioneered simultaneously in 1912 by W. L. Bragg and Max von Laue, and was applied to electron diffraction in 1927.

W.L. Bragg proposed that waves incident on crystalline materials would only constructively interfere under certain conditions.

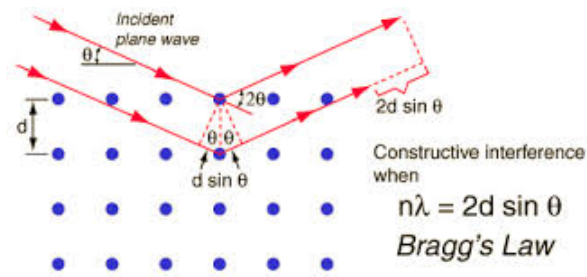


Figure 4. Bragg's law. If the path difference,  $2d \sin \theta$ , is equal to an integer number of wavelengths,  $n\lambda$ , the waves will constructively interfere.

Bragg's law for crystalline materials states that two waves reflecting off different parallel planes in the crystal lattice (oriented horizontally in Figure 4) will constructively interfere if the path difference is equal to an integer number of wavelengths. This will be discussed in section 2.3.2.4 Bragg Diffraction. W.L. and W.H. Bragg (son and father) tested and confirmed the Bragg hypothesis in 1912 using x-rays and crystal powder.

That same year, Max von Laue was independently working on his model of wave-particle interaction within crystals. The von Laue model views the crystal lattice as an array of individual atoms that act as scattering centers (as seen in Figure 5), rather than as a set of parallel planes.

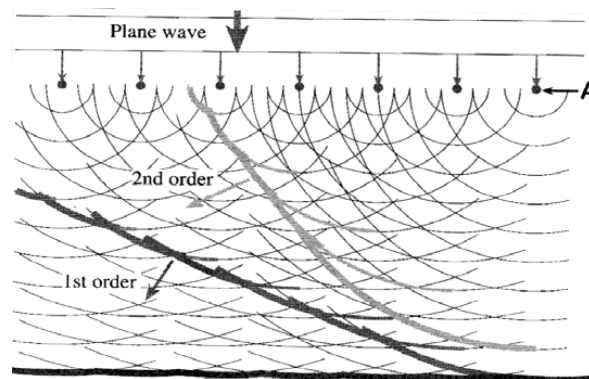


Figure 5. When a plane wave is incident on a periodic array of atoms in a specimen, the atoms act as scattering centers for the diffracted waves. See Figure 17 for more detailed explanation.

Von Laue also successfully tested his hypothesis that x-rays would be diffracted by a crystal powder. Following these discoveries, the field of X-ray Diffraction (XRD) rapidly advanced and expanded. Because of DeBroglie's work on the wave-particle nature of electrons, the Bragg and von Laue models could be applied to another emerging field—Electron Diffraction.

The earliest applications of electron diffraction in crystalline powders (forming patterns of concentric rings) were by Davisson and Germer in 1927. Heidenreich was the first to thin metals to electron beam transparency in 1949. This expanded the possibilities of electron diffraction analysis beyond powders to electron beam transparent crystals.

#### *1.4.2 Selected Area Electron Diffraction (SAED or SAD)*

Selected area electron diffraction (SAED) is a technique used in TEM to determine the crystal lattice spacing and orientation within the specimen. A parallel beam of electrons is incident on the sample, and a small area is selected to form a diffraction pattern.

When the electron beam encounters the crystalline structure of the sample, the beam is diffracted and forms an array of dots in the diffraction plane according to the constructive interference parameters outlined by both the Bragg and von Laue models. The diffraction pattern forms between the objective lens and the image plane. The objective lens focuses the scattered beam in such a way that all of the transmitted electrons scattered at a specific angle are focused together, forming a spot that corresponds to that scattering angle. SAED is further explained in section 2.4.1 Selected Area Electron Diffraction (SAED).

SAED can be used to analyze smaller areas than XRD. X-ray diffraction is limited by the area of the sample exposed to the incident beam. If the crystal size is smaller than the area of beam exposure and individual crystal characteristics are of interest, the information gained is limited. Electron diffraction uses smaller wavelengths and can target a smaller area on a sample. SAED can be used to analyze areas of about 4  $\mu\text{m}$ .

Electrons are diffracted more strongly than x-rays because the interaction is with the nucleus of the atoms in the sample rather than the electron cloud. This leads to shorter exposure times, and means that the sample can be rotated and the pattern observed simultaneously in order to observe diffraction

from different crystal orientations. The strong diffraction also means that there is not a big difference in relative intensity between the incident beam and the diffracted beam. This makes it impossible to identify the position of atoms in a unit cell using the Born Approximation[14], as is done in neutron diffraction and XRD.

#### *1.4.3 Convergent Beam Electron Diffraction (CBED)*

Convergent beam electron diffraction (CBED), developed by Kossel and Möllenstadt in 1939[17], is another diffraction method that focuses an electron beam onto the sample from a range of angles ( $\alpha > 10^{-3}$  rad) instead of using a parallel beam. This method produces a pattern with information from multiple plane spacings and orientations in one image.

CBED allowed for even smaller areas of the sample (on the order of nanometers) to be analyzed. It also opened the door to a more precise determination of atomic structure using electron diffraction.

The relative intensity limitation of SAED that made it impossible to determine precise atomic positioning was overcome by the development of CBED.[17] CBED diffraction patterns have higher angles of diffraction with lower relative intensities, and therefore can be used to determine atomic position.

### **1.5 History the JEOL 100CX TEM at Houghton College**

The JEOL 100CX TEM was donated to Houghton College by Kodak in 1991. The microscope was primarily used by Dr. Boone of the Biology department from 1991 until 2000. Dr. Boone operated and maintained the TEM in order to obtain images for microbiology. He kept a journal of procedures, problems, and repairs until he stopped working with the microscope in 2000.

The TEM was chosen to be the basis of a Physics Project Lab research project by Dr. Brandon Hoffman in the fall of 2006. Student Bruce Mourhess first worked on the project with Dr. Hoffman from September 2006 through December 2006. Mourhess and Dr. Hoffman worked on the pneumatic system, the water cooling system, and the rotary pumps. These systems were all in working order in February 2007 when the author, Daniel Ballard, succeeded Mourhess and began work on the TEM project with Dr. Hoffman. The rotary pumps were functional, but the pressure in the column chamber of the TEM was not going lower than about  $4.0 \times 10^{-1}$  Torr.

## Chapter 2

### THEORY

#### 2.1 Introduction

There are four related areas of theory that come together in order to understand the function and capabilities of a Transmission Electron Microscope: the wave/particle dual nature of the electron, the complex set of electron/matter interactions that arise from this dual nature, the analysis techniques used to characterize such interactions, and the electron beam technology utilized to control and interpret these interactions.

#### 2.2 Wave/Particle Duality

An electron is a charged particle that can be accelerated by electric and magnetic fields and thereby undergo a change in momentum and energy. An electron is also a wave. As a particle, it can be deflected by the electric field of another negatively charged electron or a positive nucleus. As a wave, it can be diffracted and result in interference patterns. These diffraction patterns, changes in energy, and deflections can all be used to find information about the atomic structure of materials.

The characteristic wavelength ( $\lambda$ ) of an electron is a key factor in determining the resolution capabilities of the microscope. The resolution of a microscope is its capability to distinguish between two discrete points on the specimen. A higher resolution means smaller objects can be imaged clearly, and smaller wavelengths leads to higher resolution.

##### *2.2.1 Relating Electron Energy to Wavelength*

DeBroglie's relations combined with some energy calculations provide a way to measure  $\lambda$  for electrons accelerated through a given potential drop ( $V$ ).

In TEM, the electron gains momentum by being accelerated through a potential drop  $V$ , giving it a potential energy of  $eV$ , where  $e$  is the charge of the electron  $-1.602 \times 10^{-19}$  Coulombs. For electrons accelerated through 100 KeV and above, however, their speed is more than half the speed of light. Because of this, the calculations must include relativistic kinetic energy and momentum.[1]

The relation between total relativistic energy  $E$  and relativistic momentum  $p$  for a particle is

$$E^2 = p^2 c^2 + m_0^2 c^4 = p^2 c^2 + E_0^2 \quad (5)$$

where  $m_0$  is the rest mass of the particle and  $E_0$  is the rest energy of the particle. The relativistic energy equation (5) can be used to show that the relativistic momentum of the electron  $p$  is as follows (see Appendix B:

Derivation for Relativistic Momentum of an Electron):

$$p = \sqrt{2m_0 \Delta E + \frac{\Delta E^2}{c^2}} \quad (6)$$

where the change in energy  $\Delta E = E - E_0$ . In this case, the change in energy of the electron is going to be due to the accelerating potential  $V$ . The electrical potential energy  $eV$  must equal the kinetic energy of the electron once it has been accelerated, therefore we can substitute  $\Delta E = eV$ . Relativistic momentum in terms of the accelerating potential would then be

$$p = \sqrt{2m_0 eV + \frac{(eV)^2}{c^2}}. \quad (7)$$

In order to find  $\lambda$  the following de Broglie wavelength is utilized,

$$\lambda = \frac{h}{p} \quad (8)$$

where  $h$  is Planck's constant ( $6.626 \times 10^{-34}$  N m s) and is  $p$  the momentum of the electron.

If  $p$  from the relativistic equation (7) is used to find  $\lambda$ , what results is an expression for  $\lambda$  in terms of the accelerating voltage  $V$  of the electron microscope. If we can measure  $V$  we can calculate  $\lambda$  for the electron because all the other constants are known,

$$\lambda(V) = \frac{h}{\left[2m_0 eV + \frac{(eV)^2}{c^2}\right]^{1/2}} \quad (9)$$

thereby giving the relativistic wavelength for an electron with a given energy.

### 2.2.2 Relating Wavelength to Resolving Power

The wavelength of visible light is on the order of  $10^{-7}$  m. Due to the discovery that electrons also behave like waves, and the corresponding wavelength of high energy electrons is smaller than visible light waves, electron beams can theoretically resolve images of much smaller objects than can be resolved by light waves.

The image resolution of a microscope depends on the resolving power of the instrument. The resolving power is the minimum distance between two physical points on the specimen such that those points can be seen as clearly separate and distinct on the magnified image produced. The theoretical calculations for the resolving power of each type of microscope are outlined in this section.

For an optical microscope, the resolving power  $d$  is calculated as follows:

$$d = \frac{0.61\lambda}{\mu \sin\theta} \quad (10)$$

where  $\lambda$  is the wavelength of light,  $\mu$  is the refractive index of the object space, and  $\theta$  is the half-angle of the cone of light that can be accepted into the aperture as seen in Figure 6.

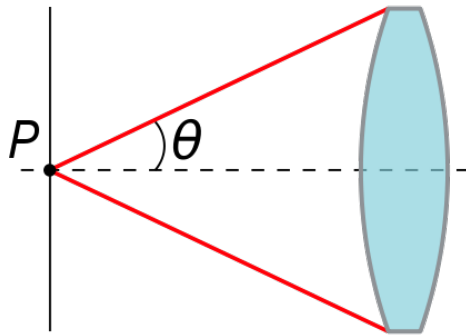


Figure 6. Optical lens diagram showing  $\theta$ , the half-angle of the light cone accepted into the aperture.

For an optical microscope with two lenses, the equation is modified as follows:

$$d = \frac{0.61\lambda}{\mu_1 \sin\theta + \mu_2 \sin\theta}. \quad (11)$$

Visible light has wavelengths in the range of 400-700 nm. The optimal parameters for maximum resolving power are  $\lambda = 400\text{nm}$  for violet light,  $\mu_1 = 1.0$  for air,  $\mu_2 = 1.56$  for a condenser lens in oil, and  $\theta \approx 70^\circ$  for the maximum light-gathering angle of an optical lens. These parameters lead to a maximum resolution for a light microscope that is approximately 100-200nm.

For the electron microscope, equation (10) can be used as a starting point to find the resolving power. For the electron microscope, the aperture angle is very small, and can be approximated using the small angle approximation  $\sin \theta \approx \theta$ :

$$d = \frac{.061\lambda}{\theta}. \quad (12)$$

Therefore, the resolving power for a given electron energy can be determined using the wavelength from Equation (9). Figure 7 shows calculated  $\lambda$  values for accelerating voltages from 1V to 1 MeV. The 100CX uses accelerating voltages in the range of 0 to 100 keV.

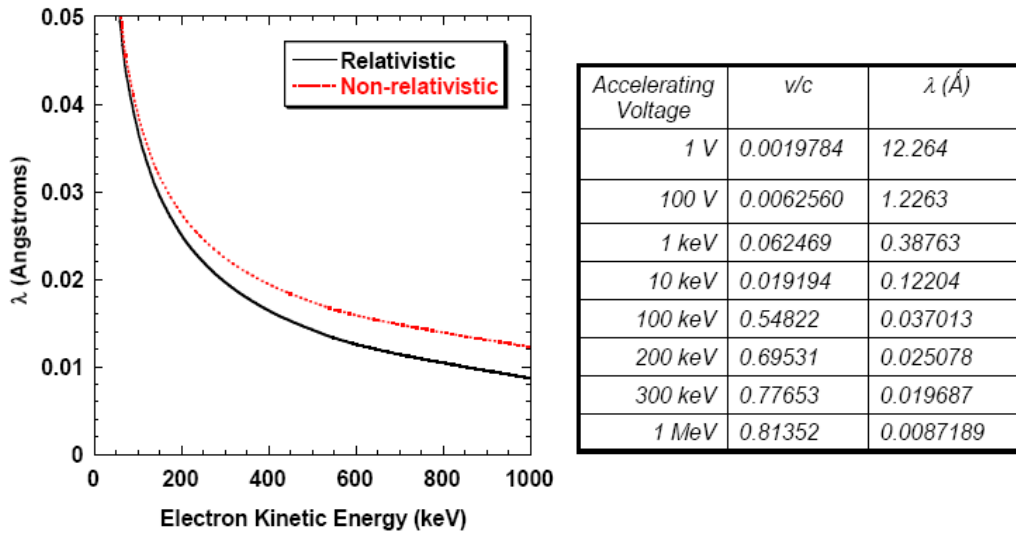


Figure 7. Relativistic and non-relativistic  $\lambda$  for electrons with energies from 1 eV to 1 MeV. The theoretical wavelength of an electron accelerated through a potential difference of 100 keV is 0.037013 Å. Taken from [18].

There are other factors that affect resolving power such as spherical aberration and diffraction limits. Even with these limitations, the resolving power of an electron microscope is much higher than that of an optical microscope. TEMs can resolve objects in the range of  $10^{-3}$  to  $10^{-10}$  m, an advantage of up to four orders of magnitude over optical microscopes.[18]

### 2.3 Electron/Matter Interaction

All information gained through TEM analysis results from electrons interacting with the sample in some way. Electrons can be either scattered as particles through Coulomb interactions with other electrons or protons (nuclei) in the sample, or they can be diffracted as coherent or incoherent waves. These scattered particles are transmitted through the sample and detected by sensors or viewed on a phosphor screen and analyzed. In order for an image to be formed, the sample has to be thin enough for an electrons to pass through with sufficient intensity to be sensed and form an image. This electron transparency thickness depends on the Z-number of the atoms in the sample and the energy of the incident electrons. For a 100keV accelerating voltage, samples with thickness of < 100 nm should be used.[19] Figure 8 shows various types of electron scattering associated with a thin specimen (electron-transparent) and a bulk specimen (non electron transparent).

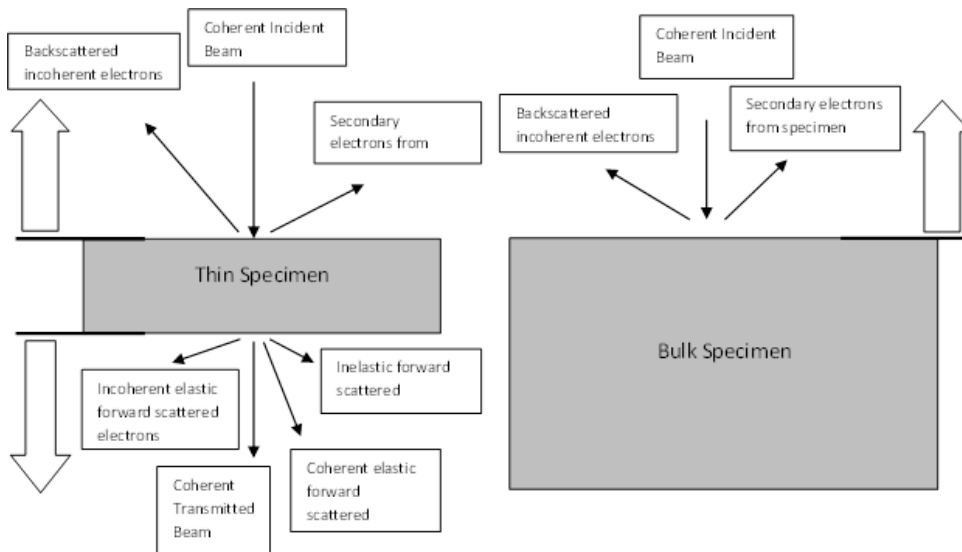


Figure 8. Electrons may be scattered at angles anywhere from 0 to 180 degrees with respect to the incident beam. A thin specimen (a) that transmits electrons is known as electron transparent. Those scattered between 0 and 90 degrees are known as forward scattered electrons, and those scattered between 90 and 180 degrees are known as backscattered electrons. The majority of information gathered through Transmission electron microscopy comes from detection and analysis of the forward scattered electrons. Because of this, thin specimens (a) that are electron transparent are used. Bulk specimens (b) are more useful in surface topography applications such as scanning electron microscopy (SEM).

### 2.3.1 Scattering as Particles

Electrons can be scattered from a specimen as a result of classical Newtonian forces between the electrons and the particles in the specimen.

#### 2.3.1.1 Introduction to Coulomb Scattering

When an electron enters a sample, its interaction with the atoms in the sample can be characterized as electron-cloud interaction or nucleus interaction as seen in Figure 9.

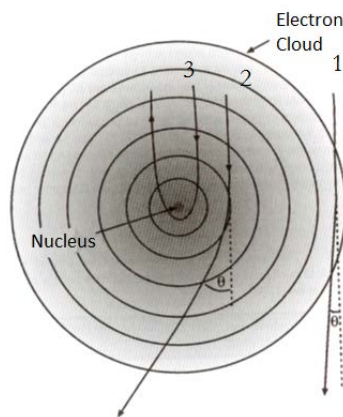


Figure 9. Electron particle scattering due to Coulomb force. Electron cloud scattering (1) results in a low scattering angle. Scattering due to interaction with the nucleus (2,3) leads to higher scattering angles up to 180 degrees.

When electrons are scattered as particles, the Coulomb force and the change in velocity that results will vary and the probability of scatter at a given angle will vary depending on the specimen thickness, the energy of the electron, and the atomic number of the atoms in the specimen.

Elastic scattering occurs when the electron is scattered by the sample in such a way that it does not lose energy. Inelastic scattering occurs when the electrons lose some of their energy. Electron scattering behavior is predicted and analyzed in terms of probability.

### 2.3.1.2 Geometry of Electron Scattering

Electron scattering is observed as a pattern formed on the imaging medium. This pattern is not a direct image of the specimen, but rather the result of interactions between electrons and the atoms within the sample. The interpretation of electron-diffraction images is based on the geometric relationship between the image and the scattering events within the sample. The knowledge that is of interest in TEM imaging is which electrons are scattered in such a way that they fall inside or outside a given scattering angle  $\varphi$ . This determines whether or not they make it through an aperture or onto a detector. For this reason it is important to know the differential scattering cross-section  $\frac{d\sigma}{d\Omega}$ , which shows the angular distribution of scattering from a given atom. The differential scattering cross-section is found experimentally, and is used to calculate the scattering cross section for a given scattering angle,  $\sigma_{\varphi}$ . The scattering cross section can be used to find the probability that an electron will be scattered within a certain range of angles. Figure 10 shows the relationship between  $\varphi$  and the solid angle  $\Omega$  oriented orthogonally to the incident electron beam.

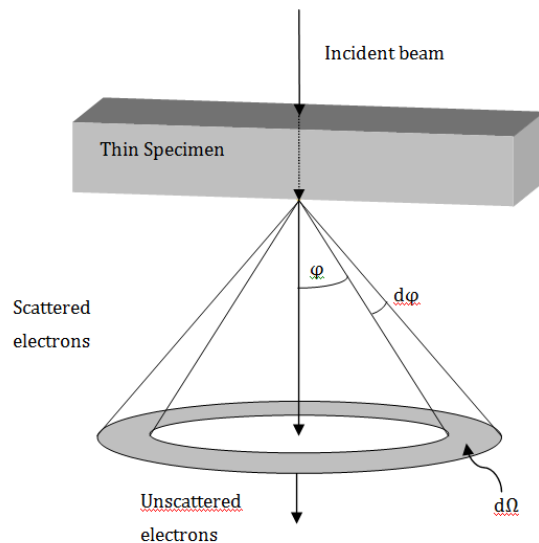


Figure 10. Geometry of electron scattering. The transmitted electrons are scattered at a semiangle  $\varphi$  with respect to the unscattered transmitted beam and solid angle  $\Omega$  measured on the plane normal to the transmitted beam. A small change in semiangle,  $d\varphi$ , will correspond to a small change in solid angle  $d\Omega$ .

The relationship between the scattering semiangle,  $\varphi$ , and the solid angle,  $\Omega$ , can be found by computing the following double integral in spherical coordinates:

$$\Omega = 2\pi(1 - \cos \varphi). \quad (13)$$

With a few more steps the differential scattering cross section  $\frac{d\sigma}{d\Omega}$  can be found.

The derivative of  $\Omega$  is found as

$$d\Omega = 2\pi \sin \varphi d\varphi. \quad (14)$$

The relationship  $\frac{d\sigma}{d\Omega}$  can then be set up as in equation (15):

$$\frac{d\sigma}{d\Omega} = \frac{1}{2\pi \sin \varphi} \frac{d\sigma}{d\varphi}. \quad (15)$$

The differential scattering cross section is determined experimentally, and we can use it to find the scattering cross section for a given scattering angle  $\sigma_\varphi$ :

$$\sigma_\varphi = \int_\varphi^\pi d\sigma = 2\pi \int_\varphi^\pi \frac{d\sigma}{d\Omega} \sin \varphi d\varphi. \quad (16)$$

Equation (16) gives the interaction cross section for a given angle  $\varphi$ . The total cross section for an atom in the specimen would be the same integral with limits of 0 and  $\pi$ . Once  $\sigma$  for one atom is found, the combined effect of all the atoms within a given specimen, known as the scattering cross section ( $Q_T$ ) can be predicted, and then  $Q_T$  can be used to find the scattering probability from a given sample.[1] This is discussed in section 2.3.1.3 Elastic Scattering.

### 2.3.1.3 Elastic Scattering

Interaction cross section  $\sigma$  is the probability that an interaction event with a given atom will occur multiplied by the incident area. The scattering cross section  $Q$  is the interaction cross section multiplied by atoms/volume and gives us the probability of an event per sample thickness. Hall in 1953 defined the total interaction cross section ( $\sigma_T$ ) for a single atom in the specimen as the sum of the elastic and inelastic interaction cross sections:

$$\sigma_T = \sigma_{elastic} + \sigma_{inelastic}. \quad (17)$$

The elastic and inelastic cross-sections are expressed in terms of area.

For the study of microstructure in materials, elastic scattering is more useful for analysis and characterization using images and diffraction patterns. For this reason, the interaction cross section for elastic scattering ( $\sigma_{elastic}$ ) will be discussed first.

Electrons are not scattered by the atom or nucleus itself, but by the Coulomb forces resulting from proximity to the electron cloud or nucleus of the atom. Each atom has an elastic scattering center with effective radius ( $r_{elastic}$ ), where

$$r_{elastic} = \frac{Ze}{V\varphi_{atom}}. \quad (18)$$

The effective radius is directly proportional to the atomic number ( $Z$ ) and  $e$  (defined in electrostatic units). It is inversely proportional to the accelerating voltage ( $V$ ) and the minimum angle through which the electron is scattered ( $\varphi_{atom}$ ). A single atom's scattering angle  $\varphi_{atom}$  is the single atom equivalent to scattering semiangle  $\varphi$  in Figure 10. If a specific scattering angle  $\varphi$  is chosen, the effective radius of interaction to produce that scattering event can be calculated. The elastic interaction cross-section ( $\sigma_{elastic}$ ) is expressed in terms of the effective scattering center:

$$\sigma_{elastic} = \pi(r_{elastic})^2 \quad (19)$$

or

$$\sigma_{elastic} = \pi \left[ \frac{Ze}{V\varphi} \right]^2. \quad (20)$$

If  $\sigma_{elastic}$  for an individual atom is known, the total cross-section  $Q_T$  can be found by multiplying by the number of atoms in a given volume. If  $N$  is atoms per unit volume,  $Q_T$  is as follows:

$$Q_T = N\sigma_T = \frac{N_0\sigma_T\rho}{A} \quad (21)$$

where  $N_0$  is Avogadro's number,  $\rho$  is the mass density of the specimen, and  $A$  is the molar mass of the atoms in the specimen.

The probability of scattering from a specimen with thickness  $t$  is found by multiplying the total cross-section ( $Q_T$  -- conceptualized as an area) by the thickness ( $t$ ):

$$Q_T t = \frac{N_0 \sigma_T (\rho t)}{A}. \quad (22)$$

The total probability of interaction in a real specimen is more complicated, due to such phenomena as the screening effects of electron cloud, but the basic elastic scattering behavior can be predicted using these equations.[1]

In transmission electron microscopy, a single scattering event can reveal useful information about the specimen. Plural (2-20) scattering events can sometimes yield information as well, but the greater the number of scattering events, the greater the probability that the result is due to more than one type of interaction. Multiple (>20) scattering events can make analysis very difficult or impossible. Thinner samples reduce the likelihood of plural or multiple scattering. How thin is determined by the properties of the sample and the energy of the incident electrons.

The average distance an electron travels between interactions with other particles through a given sample is known as the mean free path. The mean free path is often represented by  $\lambda$ , but in this discussion,  $\lambda_f$  will be used to prevent confusion with wavelength.

The mean free path is inversely proportional to the total interaction cross-section. From equation (21),  $Q_T = N\sigma_T = \frac{N_0 \sigma_T \rho}{A}$ . In effect, this can be understood as “events per distance.” If the electron travels a greater distance through the sample, the probability that it will interact with a particle in the sample and be scattered increases. The inverse of the interaction cross-section “distance per event” is known as the mean free path,  $\lambda_f$ :

$$\lambda_f = \frac{1}{Q_T} = \frac{A}{N_0 \sigma_T \rho}. \quad (23)$$

This links the mean free path back to the interaction cross-section from equation (22). Calculated  $\lambda_f$  values for accelerating voltages between 100 keV and 400 keV (typical TEM voltages) are on the order of 10nm. Single scattering assumptions may be made for specimens with thickness of this order.

The probability of scattering from a specimen of given thickness would be

$$p = \frac{t}{\lambda_f} = \frac{N_0 \sigma_T(\rho t)}{A} = Q_T t. \quad (24)$$

If the probability is greater than one, multiple scattering or plural scattering is probable and a thinner specimen will make for clearer analysis.

### *2.3.1.4 Inelastic Scattering*

Inelastic scattering occurs when electrons lose energy and the energy is transferred or converted. Inelastic scattering gives information about composition and leads to background phenomena that must be taken into consideration when analyzing and interpreting the image. This energy could be converted into other forms such as x-rays or it could be transferred to other particles (electrons, nuclei) within the specimen. Two types of x-rays, known as characteristic x-rays and Bremsstrahlung x-rays, can result from inelastic scattering. Particle energy transfer can result in the ejection of electrons from the specimen (secondary electrons), collective vibration of the electrons within a sample (plasmons), or collective vibration of the atoms within the crystal lattice (phonons).

#### *2.3.1.4.1 Characteristic X-rays*

Characteristic x-rays are produced when an electron is ejected from an energy shell that is close to the nucleus and an electron from a higher energy shell “falls” into its place, producing an x-ray with energy equivalent to the energy difference between the electron shells as seen in Figure 11. Each atom has unique characteristic x-ray energies, making them a compositional identifier.

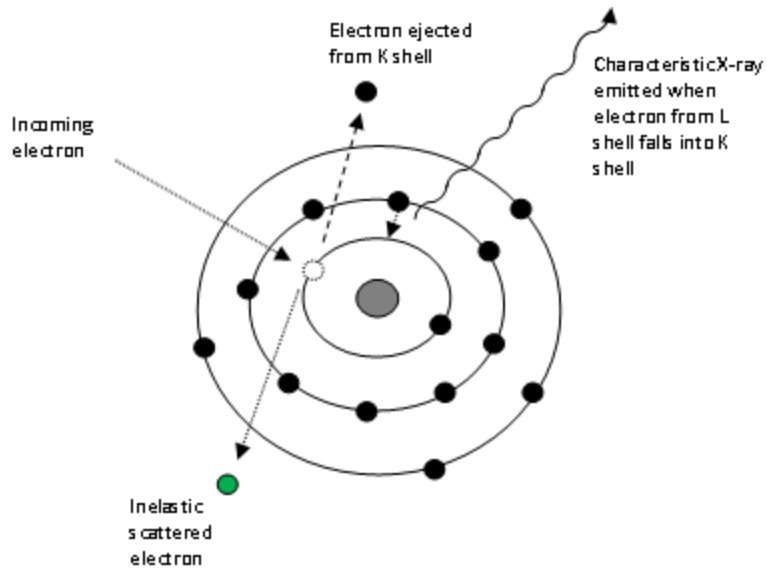


Figure 11. An incoming electron can eject an electron from an electron shell of an atom within the sample. This ejected electron is known as a secondary electron. When an inner shell electron is ejected, an electron from an outer shell will fall into its place and emit a characteristic x-ray with energy equivalent to the energy difference of the two shells.

#### 2.3.1.4.2 Bremsstrahlung X-rays

Bremsstrahlung x-rays are also known as “braking radiation,” because they produced when the incoming electron bypasses the electron shells and interacts directly with the nucleus. The Coulomb force decelerates the electron, and it will emit an x-ray with energy equivalent to the energy lost in deceleration as seen in Figure 12. Bremsstrahlung x-rays can have any energy up to the beam energy.

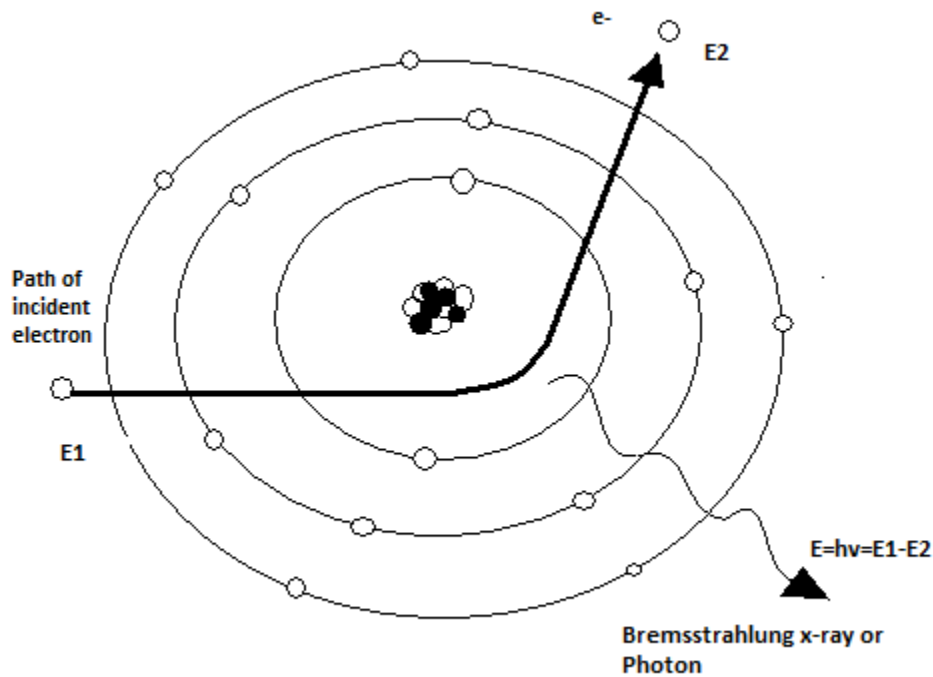


Figure 12. Bremsstrahlung x-rays given off when an electron is decelerated by coulomb forces from the nucleus of an atom in the specimen. The difference in energy between the incoming electron and the scattered electron will be given off in the form of an x-ray with  $hv = \Delta E$ .

The Coulomb force acting on the electrons will be greater with larger  $Z$  values. Equation (25) is Kramer’s cross section, which models the number of Bremsstrahlung x-rays produced by a given specimen.

$$N(E) = \frac{KZ(E_0 - E)}{E} \quad (25)$$

where  $N(E)$  is the number of Bremsstrahlung x-rays or photons at a given energy  $E$ .  $K$  is Kramer's constant [proportional to the atomic number of the element],  $E_0$  is the original energy of the electrons, and  $Z$  is the atomic number of the atom.

Kramer's cross section predicts that the number of Bremsstrahlung x-rays will vary directly with  $Z$  and that low-energy x-rays will be far more common than high-energy x-rays. Bremsstrahlung x-rays are useful in determining the type and density of elements within a sample, but are of little interest to materials scientists. Bremsstrahlung X-rays produce a background signal to be taken into consideration in the search for other x-ray signals.

#### 2.3.1.4.3 Secondary Electrons

Secondary electrons are produced when an incident electron transfers enough of its energy to an electron in the electron cloud of an atom within the sample to eject that electron from its energy shell as seen in Figure 13. Secondary electrons contribute to the topographical and compositional signals detected by the Backscatter Electron Detector (see 3.1.5.3 Backscattered Electron Detector (BSE)) used in STEM mode.

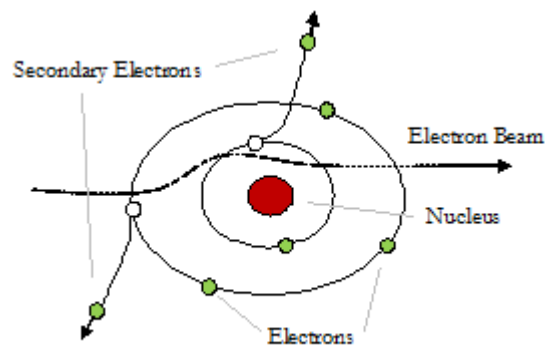


Figure 13. Secondary electrons. When the incoming electron beam interacts with electrons in the electron cloud of an atom in the sample and transfers enough energy to eject them from their place in their energy shell, secondary electrons are produced.

Secondary electrons can be grouped into two categories based on energy, namely slow and fast. Slow secondary electrons are ejected from outer shells of the atom. They come from the valence and conduction bands, which are furthest from the nucleus and take the least amount of energy to escape the Coulomb force. These slow secondary electrons have an average energy of  $\sim 50\text{eV}$ . Fast Secondary Electrons are ejected from inner shells (K,L) and may have energies up to 50% of beam energy.

#### 2.3.1.4.4 Auger Electrons

Auger electrons are the result of a two-step process. The first step is identical to the process that produces characteristic x-rays: an incoming electron excites an inner shell electron and an outer shell electron “falls” into inner shell producing characteristic x-ray. Second, the x-ray produced passes energy to an outer shell electron and ejects it. This process is also known as a “non-radiative transition” because the radiation produced is internally converted.

#### 2.3.1.5 *Sample Response to Inelastic Scattering*

Whenever an electron inelastically scatters from the sample, some of the energy can be dissipated through the sample. Plasmon and Phonon energy loss occur when an incoming electron causes oscillations within the specimen. Both phenomena affect the energy and/or trajectory of the diffracted electron beam need to be acknowledged in the analysis process.

### 2.3.1.5.1 Plasmons

Plasmons are collective oscillations of free electrons within conductive materials as seen in Figure 14. Plasmons are the most common inelastic interaction occurring in metals. The energy of a plasmon is quantized, and this leads to a characteristic plasmon wavelength of about 100nm. The energy of a Plasmon oscillation is a function of free-electron density.

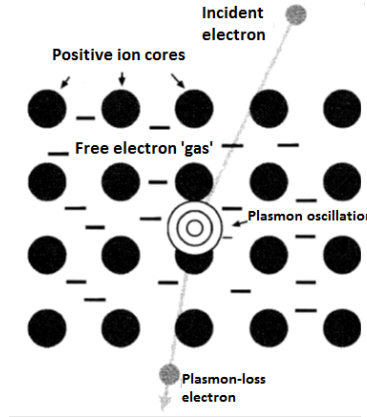


Figure 14. Plasmon oscillation. Incident electron transfers some of its energy to the free electrons within the specimen causing a collective vibration. Taken from [1].

### 2.3.1.5.2 Phonons

Phonons are oscillations in which the atoms in the crystal lattice vibrate collectively. This collective vibration, visually represented by vibrating spring-like bonds in Figure 15, is equivalent to specimen heating. A higher occurrence of phonon vibrations reduces the clarity of diffraction patterns because that the displacement of each atom from its equilibrium position breaks down the periodicity of the lattice. Since diffraction measures the atomic spacing, a variation in spacing will smudge the diffraction pattern. A cooler specimen will produce a clearer diffraction pattern. Phonons cause an energy loss of  $<0.1\text{eV}$  and have a scattering angle of  $\sim 5\text{-}15$  mrad.

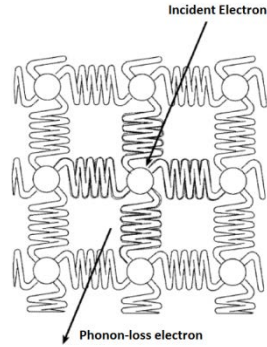


Figure 15. Phonon oscillation. Incident electrons transfer some of their energy to an atom in the crystal lattice of the specimen causing collective vibrations in the surrounding crystal structure. Taken from [1].

## 2.3.2 Scattering as Waves: Diffraction

### 2.3.2.1 Introduction

When there are multiple electron paths within a beam, the electron waves can be in phase or out of phase with each other to varying degrees. Coherent electron waves are in phase, incoherent waves are out of phase, and degrees of phase shift in between can be characterized as partially coherent.

Electron waves are diffracted in a similar manner to visible light waves. Light waves are diffracted when they pass by fine edges, through slits or through small apertures as in Figure 16.

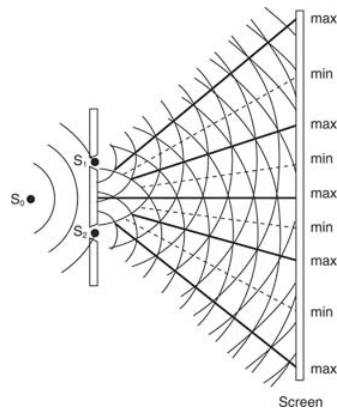


Figure 16. Incident waves emanating from a single source are diffracted as they pass through two slits. These slits essentially form two point sources and the waves that emanate from them will constructively interfere when they are in phase and will destructively interfere when out of phase, creating a series of bright and dark areas on a luminescent screen.

When a wave front encounters a barrier with parallel slits, the slits act as separate point sources as the wave is propagated through the slits in the barrier. These point sources produce waves that interact in such a way that they will form a pattern of constructive and destructive interference based on the wavelength of the propagated wave and the separation distance of the slits.

Electron waves are diffracted in a similar manner when they encounter a regular arrangement of atoms in a sample. The atoms in metals and some other solids form regular patterns called crystal lattices in the solid state. These lattices or regular patterns may or may not continue unbroken throughout the material. If they continue unbroken they are known as single crystals. Large single crystal materials like gems and diamonds may exhibit this regularity on a macro scale visible with the naked eye. Crystalline materials may also be made up of many small crystals. This means that the regular pattern may extend throughout a given volume, then be interrupted and start another regular pattern. These adjacent crystals can vary in size and orientation and may be randomly oriented or have preferred orientation(s).

An electron beam can be conceptualized as a coherent plane wave incident on a regular pattern of atoms which act as scattering centers much like narrow slits in the diffraction of light, as in Figure 17. Instead of parallel slits that form a two dimensional interference pattern, the electron beam encounters

a three dimensional array of atoms that effectively act as point sources. A two dimensional model can be used to demonstrate this type of diffraction.

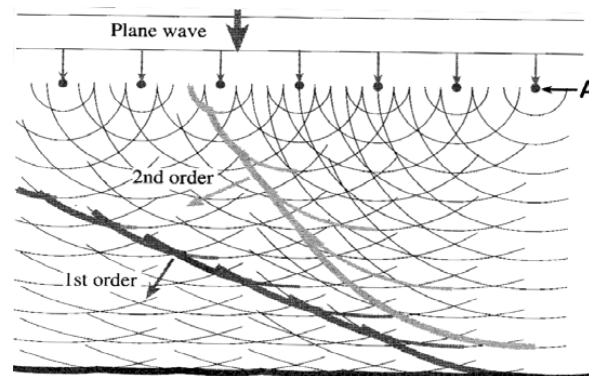


Figure 17. When a plane wave is incident upon a line or plane of scattering centers (atoms, nuclei, electron clouds) the original plane wave is transmitted (called the 0th order). The wave fronts from the other scattering centers constructively interfere to form 1st order and 2nd order plane waves with different  $\vec{k}$  vectors, or directions of propagation[1]. The  $\vec{k}$  vectors are numbered based on how much they differ from the original wave front.

### 2.3.2.2 Crystal Lattice Structure

A crystal lattice is a regular repeating pattern of atoms (see Figure 18). The unit cell is the smallest 3-dimensional section of a unique lattice that will preserve the lattice pattern if repeated.

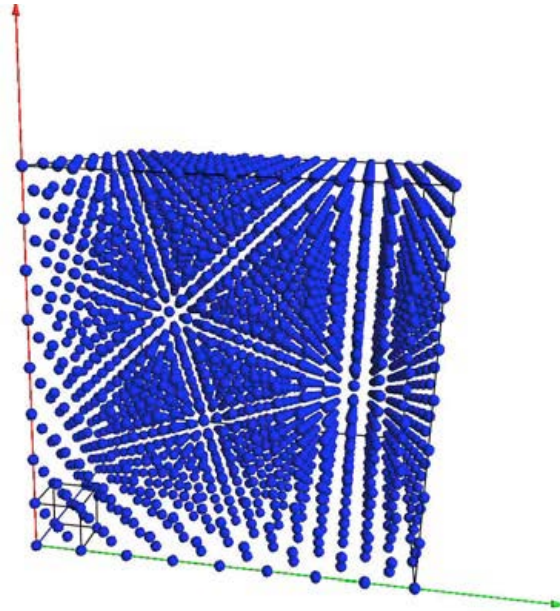


Figure 18. The unit cell in at the origin repeats in x, y, and z-directions forming a regular 3-dimensional periodic array of atoms known as a crystal lattice. Taken from [20].

This periodic array of atoms in a lattice structure forms planes called lattice planes. Lattice planes are of particular importance in TEM. A lattice plane is defined by three non-collinear atoms in the crystal lattice. The Miller index system is method that is used to define and compare these planes. A particular plane is defined by the points of intersection with the x, y, and z-axes of the plane that is closest to the origin. The reciprocals of the three intersection points  $\left(\frac{1}{x} \frac{1}{y} \frac{1}{z}\right)$  are known as the Miller index (h k l) for a lattice plane. For a primitive cubic crystal structure, a plane that includes the three atoms that are each one lattice parameter (see Figure 19) out on the x, y, and z-axes respectively would

be called the (1 1 1) lattice plane. Figure 20 shows lattice planes corresponding to Miller indices (1 0 0) and (0 2 2).

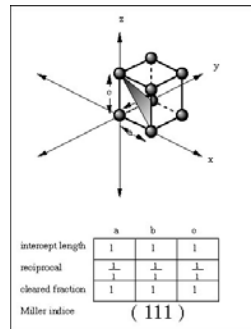


Figure 19. The lattice plane closest to the origin will pass through the x, y, and z-axes at points that are distances a, b, and c from the origin respectively. The corners of the unit cell are at a, b, and c and these are known as the lattice parameters. One lattice parameter in each direction is given a value of 1, and therefore a plane intersecting at a, b, and c would intercept at lengths 1, 1, 1. The Miller index for the plane (h k l) is found by taking the reciprocals of the distances a, b, and c respectively and simplifying to integer values. Each unique plane has a unique set of Miller indices.[21]

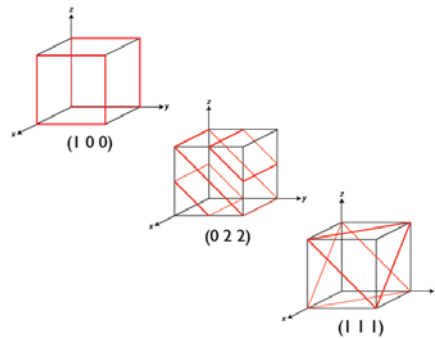


Figure 20. Examples of Miller indices for three different lattice planes in the same crystal lattice. Top left shows a plane that only crosses the x-axis and the closest point of intersection that is not the origin is where  $x=1$ , no intersection can be conceptualized as an intersect at  $\infty$ , resulting in a reciprocal of 0, therefore the plane is defined as (1 0 0). Middle shows a plane that does not intersect the x-axis and intersects at  $y = \frac{1}{2}$  and  $z = \frac{1}{2}$ , therefore defined as (0 2 2). Bottom right shows a lattice intersecting at three corners of the cube at  $x,y,z=1$  defined as the (1 1 1) lattice plane.[20]

### 2.3.2.3 Von Laue Diffraction Model

Von Laue developed a theory for constructive diffraction through a regular crystal lattice by modeling the atoms within a crystal lattice structure as scattering centers.

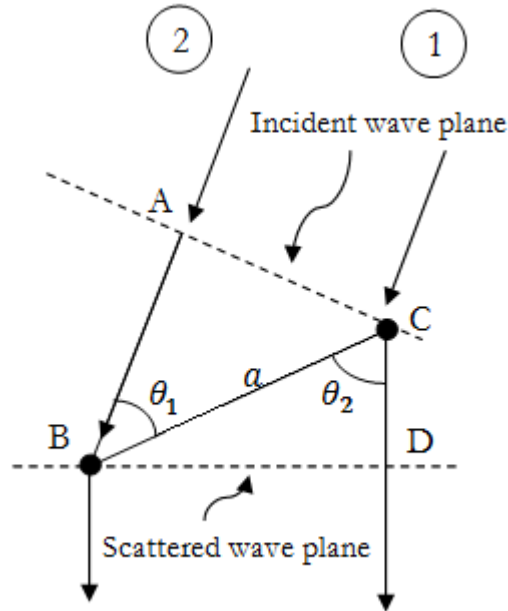


Figure 21. The geometry of the Von Laue scattering model. The distance between atoms  $a$ , the angle between the incident wave plane and the atomic plane  $\theta_1$ , and the angle between the scattered wave plane and the atomic plane  $\theta_2$  are shown. Wave 1 and wave 2 are in phase at wave front  $\overline{AC}$ . At this point, wave 1 is scattered by point C and wave 2 must travel distance  $\overline{AB}$  before it is scattered by point B. After scattering, wave 1 travels distance  $\overline{CD}$  after which it again runs parallel to wave 2. The total path difference is then  $\overline{AB} - \overline{CD}$ . If this distance is equal to an integer number of wavelengths  $h\lambda$ , then waves 1 and 2 will constructively interfere.

The path lengths can be related to the atomic spacing  $a$  through the following relations:

$$\overline{AB} = a \cos \theta_1, \quad (26)$$

$$\overline{CD} = a \cos \theta_2, \quad (27)$$

and

$$\overline{AB} - \overline{CD} = a(\cos \theta_1 - \cos \theta_2) = h\lambda. \quad (28)$$

Equation (28) is the condition for constructive interference when  $h$  is an integer. The one-dimensional example in Figure 21 can be repeated two more times in 3 dimensions to find the  $h, k, l$  Miller indices of the crystal lattice. This results in three equations, one for each dimension of crystal lattice spacing:

$$a(\cos \theta_{1h} - \cos \theta_{2h}) = h\lambda, \quad (29)$$

$$b(\cos \theta_{1k} - \cos \theta_{2k}) = k\lambda, \quad (30)$$

and

$$c(\cos \theta_{1l} - \cos \theta_{2l}) = l\lambda. \quad (31)$$

A diffraction beam will be formed when all three  $(h,k,l)$  von Laue equations are satisfied simultaneously.

#### 2.3.2.4 Bragg Diffraction

Electron wave diffraction can also be conceptualized as incident waves being reflected from atomic plane surfaces (see Figure 22). Bragg's law is used to determine the pattern of constructive interference that will result from electromagnetic waves being reflected from parallel atomic planes a distance  $d$  apart. Bragg's law has been used very effectively in X-ray diffraction to characterize the structure of materials.

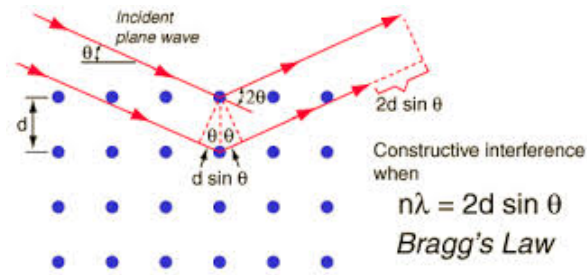


Figure 22. Bragg's Law. When EM waves are incident on a surface that has a crystal lattice structure, some waves are reflected from the first plane of atoms and some are transmitted through the first plane and reflected from the 2<sup>nd</sup> plane with plane spacing  $d$  between parallel planes. If the waves have angle of incidence  $\theta$  then the wave that is reflected from the 2<sup>nd</sup> plane travels a distance  $2d\sin\theta$  further than the one reflected from the first plane, and is therefore a distance  $2d\sin\theta$  out of phase with respect to the first reflected wave. If this phase difference is equal to an integer number of wavelengths  $n\lambda$ , then there will be constructive interference.

The Bragg model is not as accurate as the von Laue model in terms of portraying what is really happening on the atomic scale. Even so, it represents a mathematically accurate condition for constructive interference based on atomic plane spacing and the mathematical equivalence of the von Laue scattering center model and the Bragg model has been demonstrated[22]. The relative simplicity of the Bragg model makes it a commonly used alternative to the von Laue equations.

## 2.4 Imaging and Analysis Techniques based on Electron Scattering

When electrons are scattered by a sample in the TEM, they are detected and then analyzed in order to find information about the specimen. The TEM characterization techniques most commonly used in the study of thin metals are selected area electron diffraction (SAED) and convergent beam electron diffraction (CBED). Scanning transmission electron microscopy (STEM) is a TEM function that is used in conjunction with other imaging and analysis techniques to analyze a small area of the sample point by point in rapid succession. Other characterization techniques include the detection and analysis of characteristic x-rays, secondary electrons, and Bremsstrahlung x-rays. These types are not as useful in TEM analysis of thin metal films, and therefore will not be discussed in depth in this section.

### 2.4.1 Selected Area Electron Diffraction (SAED)

Selected area electron diffraction (SAED) is a technique used to obtain electron diffraction patterns and to determine the crystal lattice spacing and orientation within the specimen. A parallel beam of electrons is incident on the sample, and a small area is selected to form a diffraction pattern.

When the electron beam encounters the crystalline structure of the sample, the beam is diffracted and forms an array of dots in the diffraction plane according to the constructive interference parameters outlined by both the Bragg and von Laue models. Figure 23 shows the diffraction of the incident beam forming a diffraction pattern in the diffraction plane and an image in the image plane. The diffraction pattern forms between the objective lens and the image plane. The objective lens focuses the scattered beam in such a way that all of the transmitted electrons scattered at a specific angle are focused together, forming a spot that corresponds to that scattering angle. Figure 24 gives a ray diagram comparison of a magnified image and a projected diffraction pattern.

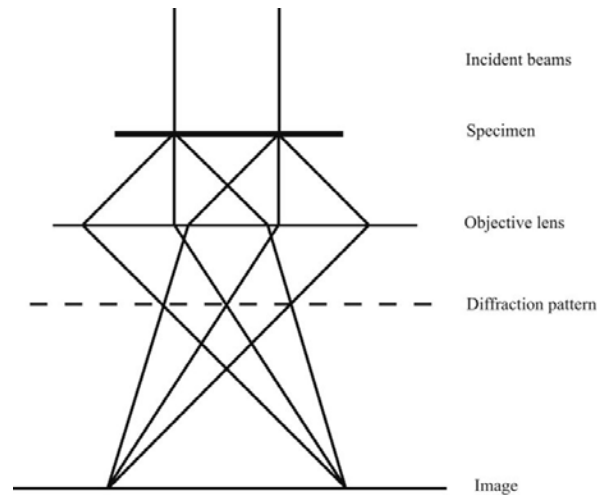


Figure 23. Selected area electron diffraction. The parallel incident electron beam is scattered in a regular geometry by the crystal planes within the specimen. Note that the objective lens focuses the scattered beam in such a way that the electrons scattered at a given angle converge to a point where the diffraction pattern is formed. The beam then passes through the plane where the diffraction pattern is formed and the electrons scattered from a given point on the specimen converge once again to form an image in the image plane.

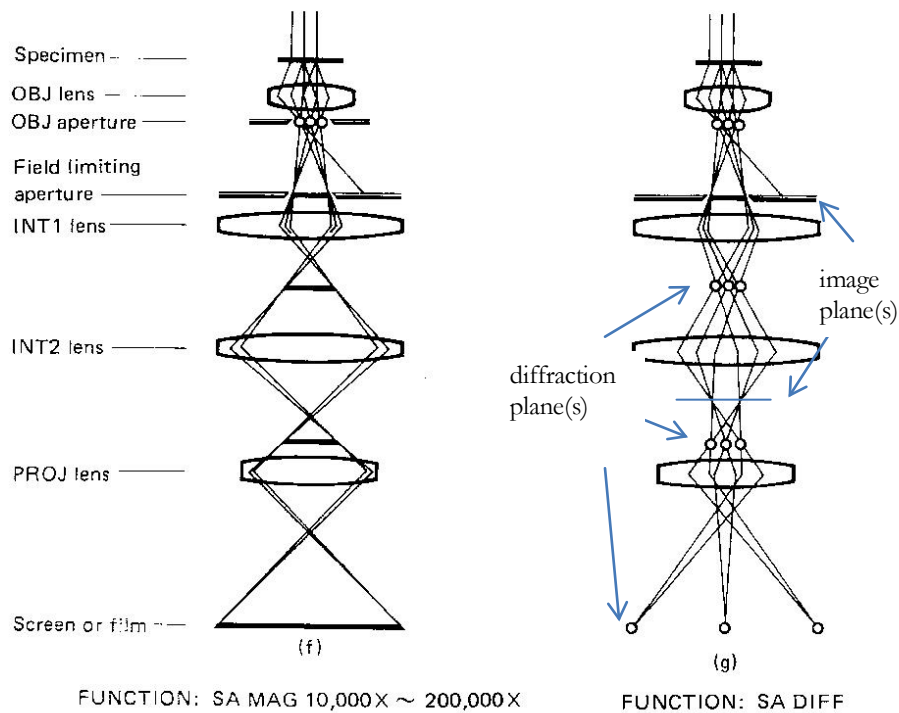


Figure 24. Ray diagrams for SA magnification (left) and SA electron diffraction (right). In both situations, a diffraction pattern is formed in the focal plane of the objective (OBJ) lens. To form an image, a beam spot is selected using the OBJ aperture and the image projected is magnified by the intermediate (INT) and projector (PROJ) lenses. At the image plane, the electrons from the same point on the sample converge. This plane shows real space image. In order to form a diffraction pattern, the diffraction pattern (instead of the image) is projected and magnified by the INT and PROJ lenses. At the diffraction plane, electrons from different parts of the sample that meet the same Laue condition all converge. This plane shows crystal orientation via diffraction pattern (spots).

SAED allows for relatively easy transition between a diffraction pattern for the selected area and an image of that area. When the diffraction pattern is viewed, the field limiting aperture (sometimes referred to as the Selected Area Diffraction or SAD aperture) is used in the image plane to create a virtual aperture at the specimen (see Figure 25). This allows the illuminated area to be virtually narrowed so that a smaller portion of the illuminated area on the specimen contributes to the diffraction pattern. In practice, the smallest apertures are  $\sim 10 \mu\text{m}$  in diameter, translating to a virtual aperture at the specimen of  $\sim 4 \mu\text{m}$ .

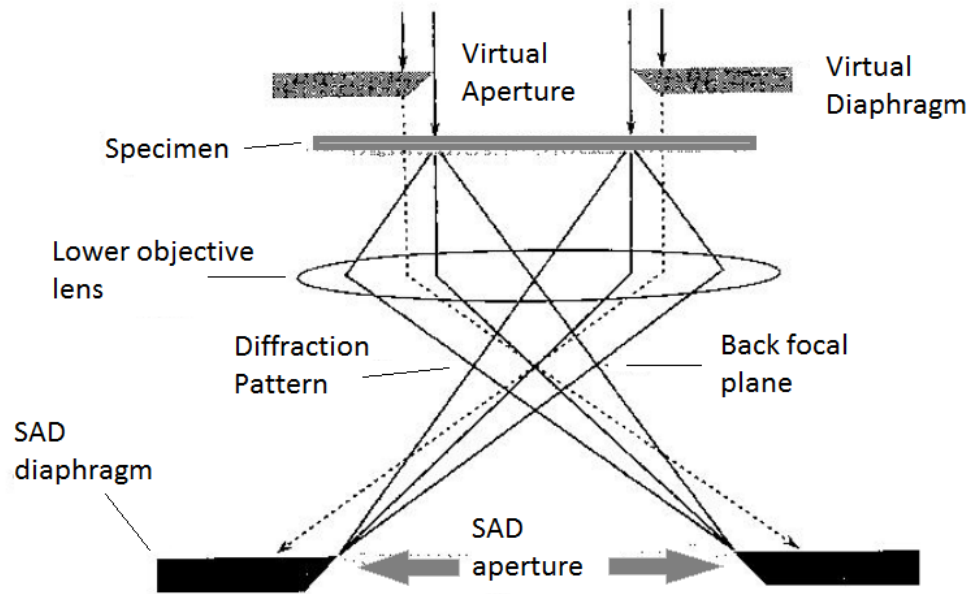


Figure 25. The field limiting (SAD) aperture. This aperture creates a virtual aperture in the specimen plane by blocking the scattered rays originating from the outer edges of the illuminated area on the specimen. Taken from [1].

In order to view an image of the selected area, the OBJ aperture is used to select either a direct beam for bright field (BF) imaging or a scattered beam for dark field (DF) imaging.[1]

During bright field imaging, a real space image of the entire portion of the sample is focused on the screen. For a dark field image, an aperture at the diffraction plane selects out a certain orientation by only allowing one spot through. Then you focus the image plane on the screen and get an image of only the parts of the sample that have that orientation.

One crystal lattice can have multiple orientations of diffracting planes, and SAED can lead to information about one plane orientation at a time. The sample must be rotated in order to image lattice planes of different orientations. Figure 26 shows different diffraction patterns resulting from various degrees of tilting in a sample of  $\text{Al}_{78}\text{Mn}_{22}$ .

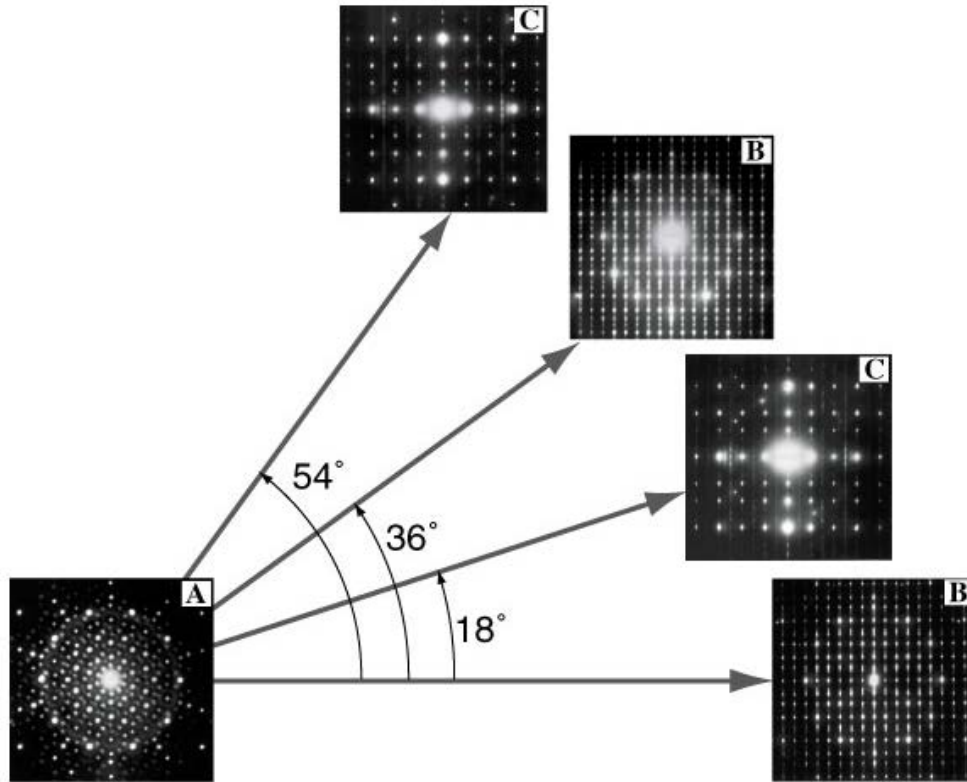


Figure 26. Different diffraction patterns are formed when a crystal of  $\text{Al}_{78}\text{Mn}_{22}$  rapidly solidified alloy is tilted 0,18,36, and 54 degrees. Taken from [23]

#### 2.4.2 Convergent Beam Electron Diffraction (CBED)

Convergent beam electron diffraction (CBED) is another diffraction method that focuses an electron beam onto the sample from a range of angles ( $\alpha > 10^{-3}$  rad) instead of using a parallel beam. This method produces a pattern with information from multiple plane spacings and orientations in one image.

A convergent beam can focus on a smaller area of the specimen than a parallel beam, making CBED a useful tool in characterizing small areas. A small spot size for a parallel beam is about 100 nm in diameter. Spot sizes as small as a few nanometers across have been achieved using CBED.

As the incident beam goes from parallel (no convergence) to larger and larger convergence angle  $2\alpha$ , the diffraction pattern changes from individually resolved spots to overlapping discs that form patterns

of bands or lines each corresponding to an  $hkl$  lattice plane within the specimen. Figure 27 illustrates this phenomenon.

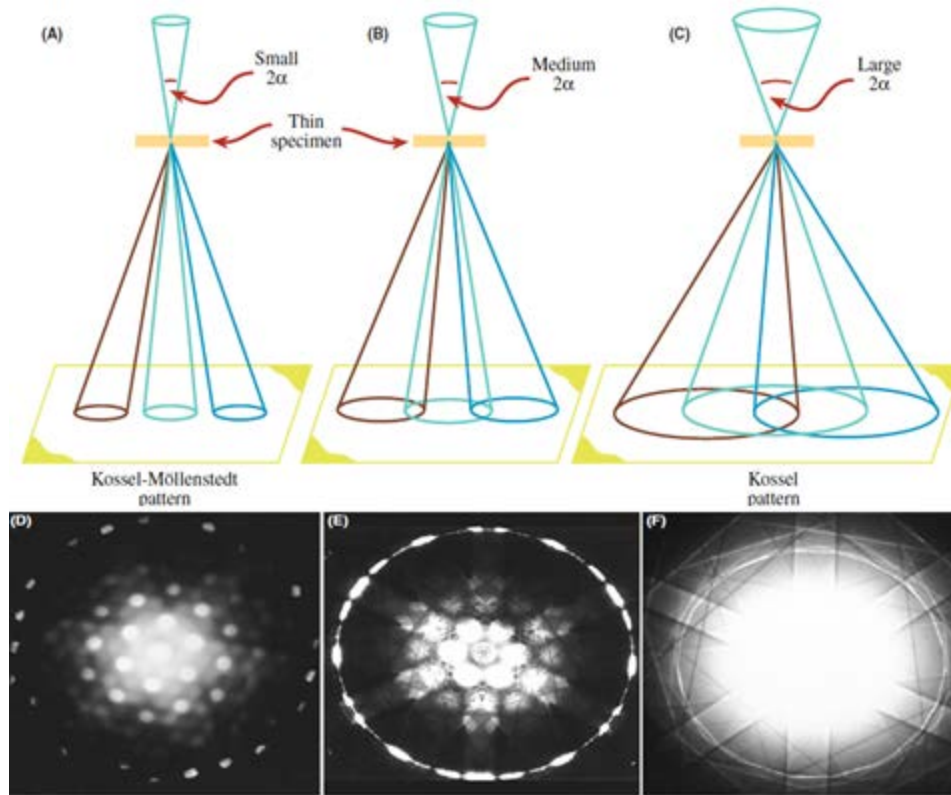


Figure 27. The effect of beam convergence on overlap of diffraction spots in CBED. As the half angle  $\alpha$  of the incident beam on the specimen increases (from A to B to C), the pattern that is formed progresses from an array of individually resolved diffraction spots (D- Kossel-Möllenstedt pattern), to a pattern with partial overlap (E), to a pattern in which all the discs overlap (F – Kossel pattern). The Condenser Lens aperture is used to change  $\alpha$ .

The Bragg diffraction from each  $hkl$  lattice plane forms lines in the image known as Kikuchi lines. These lines can only form when Bragg diffraction results from a source with a range of angles. Figure 28 shows two different sources that can result in Kikuchi lines. In CBED, the convergent beam provides this range. In other instances, inelastic scattering from a “source” within the specimen provides the range of angles required. This situation can occur in TEM with forward-scattered electrons. Electron Backscatter Diffraction (EBSD) is a technique used in Scanning Electron

Microscopy (SEM) where inelastically scattered electrons undergo Bragg diffraction and form a BSE image of Kikuchi lines.

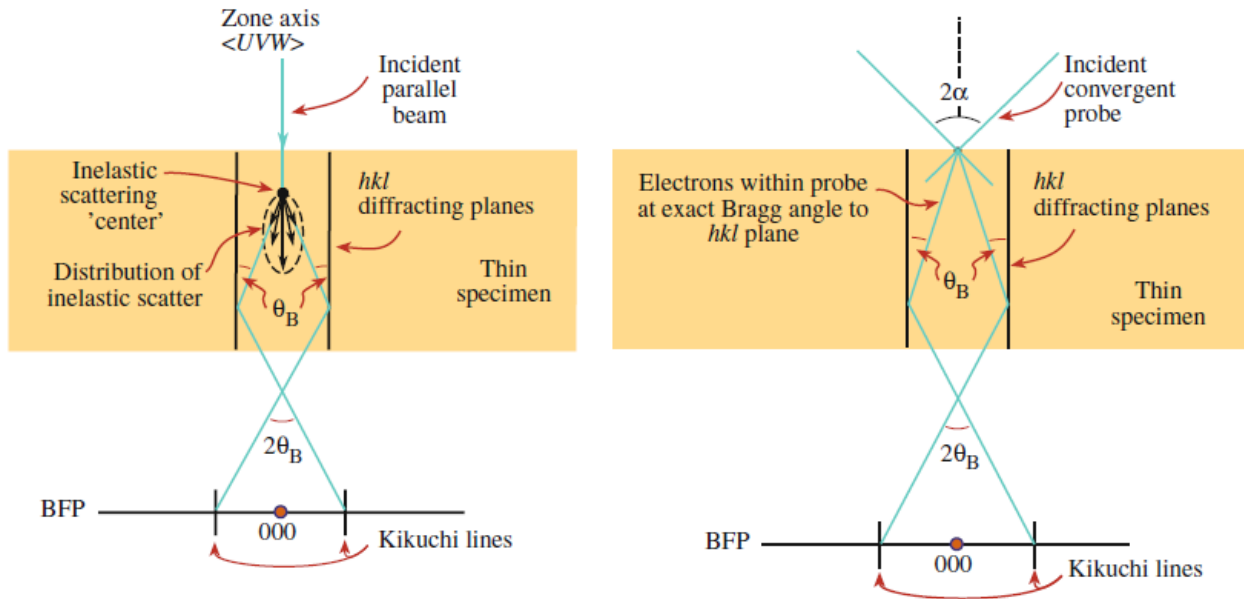


Figure 28. Kikuchi line only form when the beam interacts with the  $hkl$  diffraction planes over a range of angles. An incident parallel beam can be inelastically diffracted within the specimen (left) resulting in a range of scattering angles. An incident convergent probe (right) used in CBED introduces angles over the range of  $2\alpha$ . In both cases, the beams that match the Bragg angle  $\theta_B$  for the diffracting planes will form Kikuchi lines.

As the crystal structure is rotated, the Kikuchi patterns may exhibit different whole pattern symmetries (Figure 30) which originate from symmetries within the crystal structure of the specimen (See Figure 29).

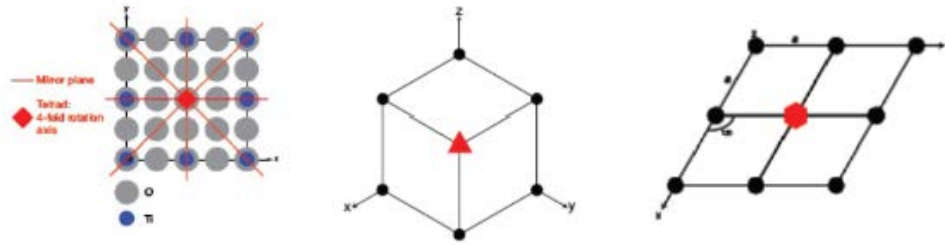


Figure 29. Rotational symmetry in the crystal lattice. A tetragonal crystal (left) has 4-fold rotational symmetry about the  $[0\ 0\ 1]$  or z-axis. A cubic crystal structure (center) has a three-fold rotational symmetry about the  $[1\ 1\ 1]$  axis. A hexagonal crystal structure (right) will have 6-fold rotational symmetry about the  $[0\ 0\ 1]$  direction or the z-axis.

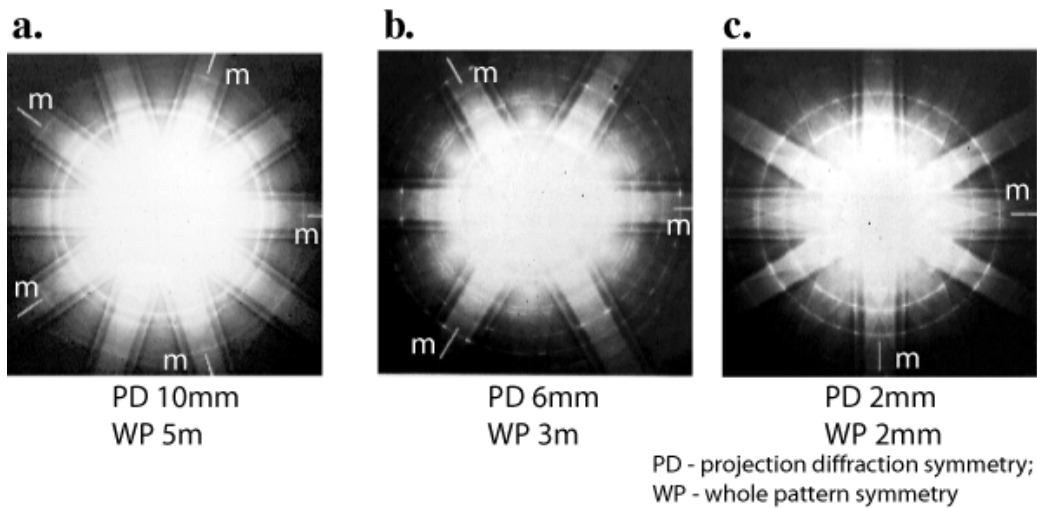


Figure 30. Three examples symmetry in CBED image patterns. CBED forms an image known as a Kikuchi pattern. This pattern is formed by intersecting bands of different intensities. Each band corresponds to an atomic plane orientation in the sample and different crystal structures and orientations will form characteristic patterns, each exhibiting unique geometry and symmetry.

The Kikuchi images formed through CBED are indexed against patterns of materials with known microstructure, including plane spacing and orientation. The plane spacings and unit cell structure and orientation of the microstructure can then be determined.[17]

The small beam spot size achieved by converging the beam makes CBED particularly useful in nano-scale analysis. CBED is used to characterize materials that are comprised of single crystals too small to be characterized using x-ray and neutron diffraction. Some examples are metastable or unstable phases, products of low-temperature phase transitions, fine precipitates, and other nano-sized particles.[23]

### 2.4.3 Scanning Transmission Electron Microscopy (STEM)

Scanning Transmission Electron Microscopy (STEM) is an analysis technique used to analyze very small areas of the sample one after the other and to compile the information in a map to learn about a larger area. STEM uses a small beam spot, or probe, to analyze small areas in the sample. This probe is scanned across a section of the sample. Information from each section is collected in series and is transmitted to a detection device (a CCD, PMT, CRT or other detector). The imaging software maps out an image based on the compiled information from each small area of the sample.

Figure 31 shows the beam path as it is deflected and re-oriented to remain parallel to the sample. The scanning coils are located above the sample and below the condenser lenses.

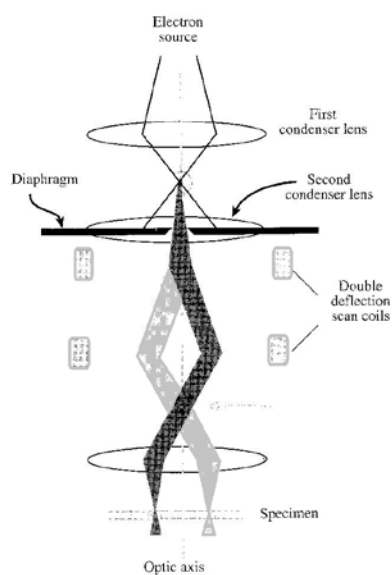


Figure 31. The scanning convergent beam remains parallel to the optic axis as it scans across the specimen in STEM mode. The double deflection coils located between the condenser lens and the upper pole piece of the OBJ lens scan the beam in such a way that it pivots in the back focal plane of the OBJ lens, thereby ensuring parallel orientation as the beam moves across the specimen.

Two sets of scanning coils deflect the beam in such a way that it pivots about the back focal plane of the objective lens, forming a parallel beam at the specimen to ensure consistent beam orientation as it is scanned across the specimen.

## *2.4.5 Other Characterization Techniques*

### *2.4.5.1 X-ray Spectrometry*

X-ray spectrometry is the analysis of characteristic x-rays given off by electron excitations within the shells of the atoms in the sample. (See section 2.3.1.4.1 Characteristic X-rays.)

### *2.4.5.2 Electron Energy Loss Spectrometry*

Electron Energy Loss Spectrometry (EELS) is another characterization technique sometimes used in TEM. Energy loss results from inelastic collisions within the specimen. (See section 2.3.2 Inelastic Scattering).

### *2.4.5.3 Bremsstrahlung X-rays*

Bremsstrahlung x-rays result from deceleration of electrons due to nucleus interaction. The amount of energy lost relative to the incident beam can give information about the composition of the sample.[24] (See 2.3.1.4.2 Bremsstrahlung X-rays.)

### *2.4.5.4 Secondary Electron Analysis*

Secondary electrons are emitted from the sample with relatively low energy. Surface topography can be determined by comparing relative intensity as the beam is scanned across the sample. For further explanation of how this technique is used in the 100CX, see section 3.1.5.3 Backscattered Electron Detector (BSE).

## 2.5 Electron Beam Technology

Three specific requirements are needed in order to image objects using an electron beam: a source for the electrons, a way to focus them and manipulate the beam to obtain different magnification levels (electromagnetic lenses), ways to detect the electrons after they have interacted with the specimen, and a medium that they can pass through that will not interfere with the beam (vacuum environment).

### 2.5.1 Electron Sources

In order to image an object with electrons, a reliable and consistent electron source is needed. The two most common sources used to produce a consistent beam of electrons are thermionic emission guns and field emission guns. The 100CX uses the former. The theory of how the electrons are released to form a beam and how the beam current and energy are controlled are outlined in this section.

#### 2.5.1.1 Thermionic Emission

The JEOL 100CX uses a thermionic emission electron source. For thermionic emission to take place, the material is heated so that the electrons have enough energy to escape. When the atoms in the material are not thermally excited, the electrons remain in the electron cloud because of the attraction of the positive charge of the nucleus. There exists a thermal energy threshold, which is different for each material, and when this threshold is surpassed, an electron can leave the orbital of its atom, and move freely either through or out of the material. This energy barrier is called the “work function” ( $\Phi$ ). When we heat a material, we can free the electrons to form a beam with a certain current. These free electrons can then be accelerated through a potential difference, forming a beam of high energy electrons.

Richardson’s Law relates the current density of electrons from the source,  $J$ , to the operating temperature,  $T$ , and work function,  $\Phi$ .

$$J = AT^2e^{-\Phi/kT} \quad (32)$$

where  $k$  is Boltzmann’s constant ( $8.6 \times 10^{-5}$  eV/K), and  $A$  is Richardson’s “constant” ( $A/m^2 K^2$ ). Richardson’s “constant” as written here actually changes by a scaling factor depending on the material.

It is sometimes written as  $A_G = \lambda_R A_0$  where  $\lambda_R$  is a scaling factor based on the material being used and  $A_0 = \frac{4\pi m k^2 e}{h^3} = 1.20173 \times 10^6 \text{ A/m}^2 \text{ K}^2$ . Materials with a high melting temperature or a low work function will yield higher current densities. Tungsten works well as a thermionic emission source because of its high melting point of 3660 K. Lanthanum hexaboride ( $\text{LaB}_6$ ) is a good electron source because of its low work function.[1]

### 2.5.1.2 Self-Biased Thermionic Emission Electron Gun

After electrons are emitted from the thermionic emission electron source, they need to be directed and accelerated in order to form a beam of a given current and energy. The Wehnelt type electron gun assembly (see Figure 32) used in the 100CX provides a steady source of electrons, regulates the emission current, and accelerates the electrons so that they form an electron beam of a given energy, measured in electron volts (eV).

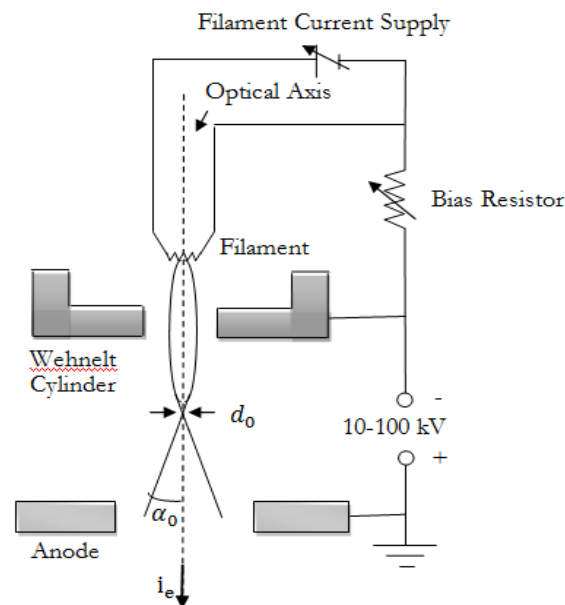


Figure 32. Self-biasing Thermionic Emission Electron gun. Electrons are emitted from the heated Tungsten filament. As emission increases, the Wehnelt cylinder becomes negatively biased with respect to the filament, which causes the Wehnelt to repel (suppress) emission. The electrons are then accelerated toward the positively charged anode and pass through the opening with energy eV.

The Wehnelt cylinder is at a negative potential of about 10-100 kV relative to the anode, which is at ground potential. The Wehnelt cylinder is also biased negatively with respect to the filament. This bias suppresses electron emission from the filament except for at the tip, where there is a small opening in the Wehnelt cap. As the electrons leave the filament, they are condensed into a beam as they pass through the Wehnelt opening, which is at a negative potential. The electron beam is focused to a point somewhere between the opening in the Wehnelt cap and the anode, and this crossover point is also known as the effective electron source ( $d_0$ ). This type of electron gun is a self-biasing gun as the bias resistor automatically adjusts the beam current to near-optimum conditions.

The beam energy can be controlled by changing the potential difference (V) between the negatively biased Wehnelt cylinder-filament combination and the anode (at ground potential). The beam current can be controlled using the filament current supply and is regulated by the circuit that includes the bias resistor.

## *2.5.2 Electromagnetic Lenses*

### *2.5.2.1 Introduction to Electromagnetic (EM) Lenses*

Optical microscopes use glass lenses in order to focus and magnify the beam of light (photons). Electrons are not refracted by glass, but rather by electric and magnetic fields, and therefore electron microscopes use electric and/or magnetic field “lenses” to focus the electron beam. The effect of these electromagnetic lenses is very close to the effect of a glass lens on visible light. Because of this similarity, optical ray diagrams are often used to illustrate electron-electromagnetic lens interactions.

### *2.5.2.2 Electromagnetic Forces and Electrons in the EM Lens*

The electromagnetic lens usually consists of a solenoid (coil of wire through which an electric current can flow) surrounded by a soft iron casing or shroud. Soft iron pole pieces are also sometimes included in order to further concentrate the field (see Figure 33). A stronger and more concentrated magnetic field will yield higher magnifications and shorter focal lengths.

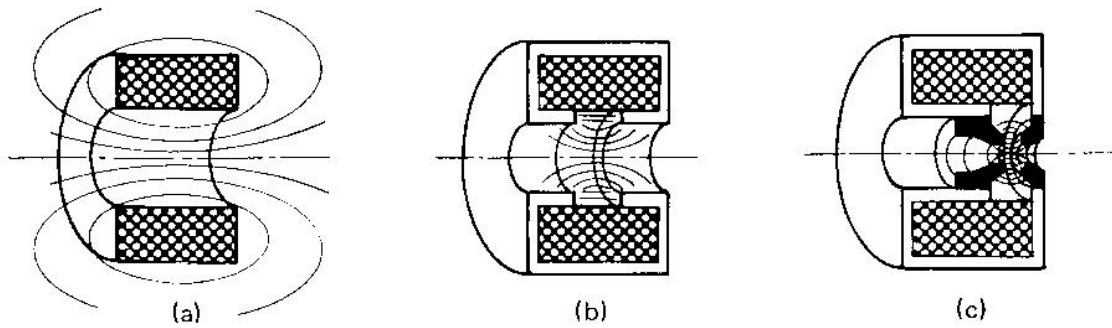


Figure 33. The concentration and strength of the magnetic field increases from (a) to (c). Figure (a) shows the magnetic field around a solenoid coil. Figure (b) adds a soft iron shroud with a gap that concentrates the field in that gap. Figure (c) adds soft iron pole pieces to narrow the diameter of the lens, further concentrating the magnetic field. Design (c) is used in lenses where high resolving power and magnification are desired.

The magnetic field created by the solenoid in a TEM forms an electromagnetic “lens” through which the electrons pass and are redirected and focused, with much the same result as focused light in an optical microscope. In a light microscope, the light is bent as it slows at the interface between mediums with differing refractive indices. In a TEM, the electron beam is “bent” through a complex series of interactions between moving electric charges and the magnetic field through which they are traveling.

Figure 34 is a cross section of a circular coil of wire (forming a solenoid) surrounded by an iron shroud. When current is passed through the solenoid, a magnetic field forms around the coil, resulting in a radially symmetric B-field. This B-field is represented by the magnetic field lines shown in the cross section. The electrons form a slightly spreading beam as they enter the magnetic field from the electron source on the left with initial velocity  $\mathbf{v}_1$ . The spreading trajectory of the electrons is exaggerated in the diagram.

The force on an electron traveling through an electric field is

$$F = q\mathbf{v} \times \mathbf{B} \quad (33)$$

where  $q$  is the electron charge ( $1.622 \times 10^{-19}$  Coulombs),  $\vec{v}$  is the velocity of the electron, and  $\vec{B}$  is the magnetic field. When the trajectory of the electron is at an angle with respect to the magnetic field lines, it will experience a force that will change its trajectory. The strength of the magnetic field will determine focal length of the lens. Higher solenoid current will increase the strength of the magnetic field and will cause a greater curvature of the path of the electrons.

The divergent electron beam enters the magnetic field, the paths of the diverging electrons are curved by the force they experience traveling through the field, and the paths converge on the other side of the electromagnetic lens at a sharp focal point.

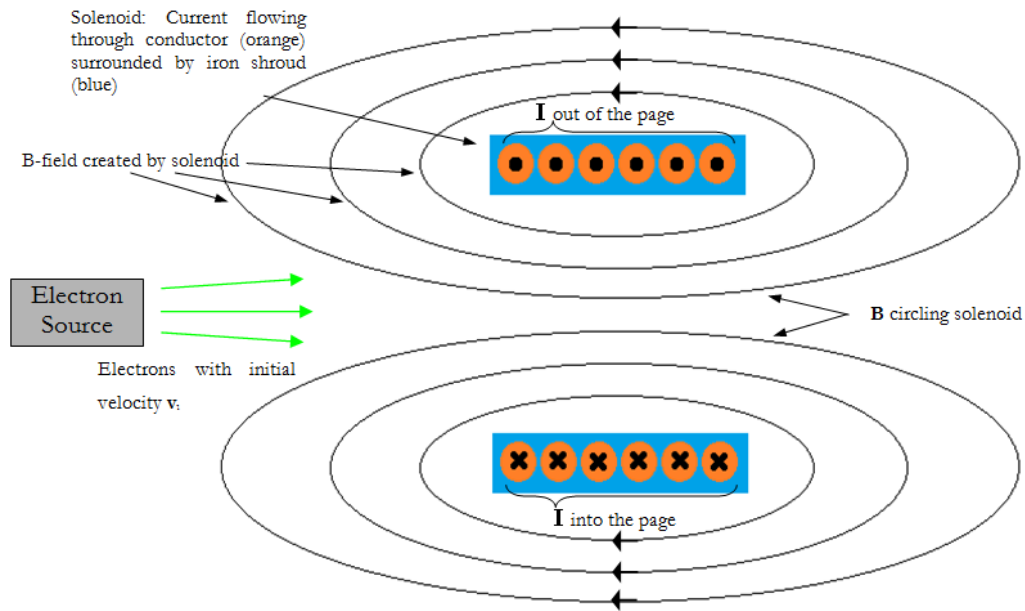


Figure 34. Cross section of an Electromagnetic Lens. This lens forms a magnetic field by passing current through a solenoid coil. The electron beam enters from the left with a slightly spreading trajectory. As the electrons pass through the B-field they are redirected and focused to a point after passing through the EM lens.

The forces that result in this focusing effect are outlined in Figure 35. It is helpful to conceptualize the forces on the electron in three zones. In reality, these zones and the effects they have on the electrons are gradual and blended one into the other, but the resulting effect is the same.

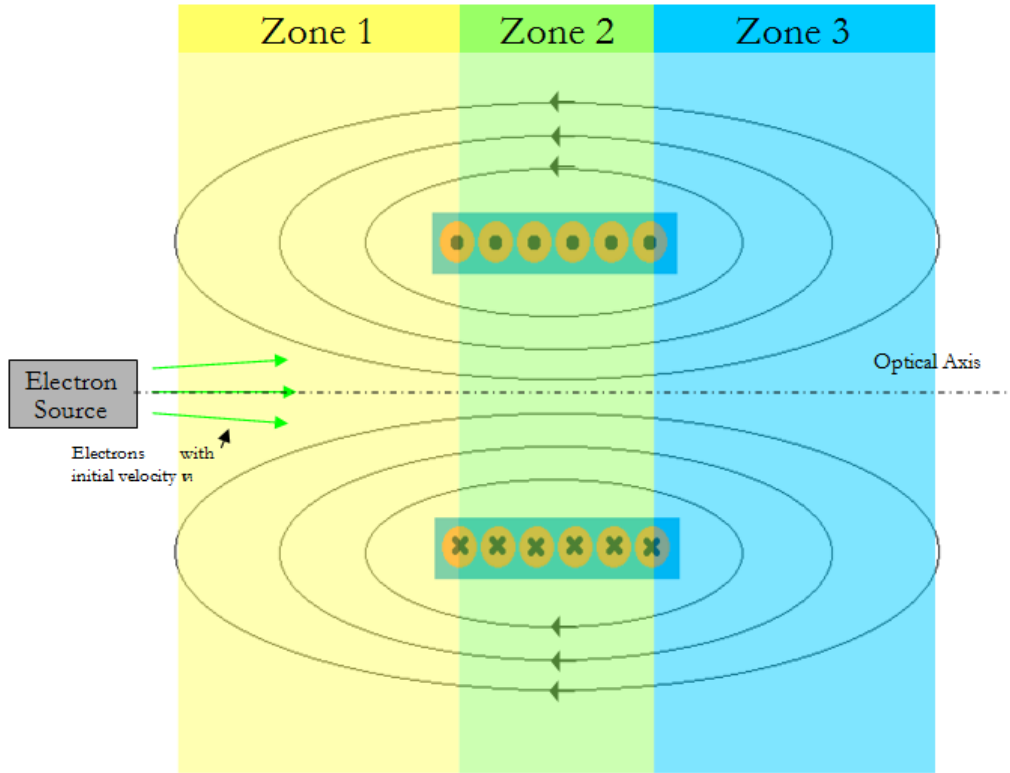


Figure 35. Electromagnetic Lens divided into three force interaction zones. The combination of the forces experienced by the electrons in each zone result in a helical path with electrons emerging from a source point and converging in a focal point after passing through the lens.

In all zones, the path analyzed is that of an electron in the upper half of the solenoid. Electrons in the lower half would experience  $\mathbf{B}_1$  and  $\mathbf{B}_3$  in the opposite direction, resulting in opposite  $\mathbf{F}_1$  and  $\mathbf{F}_3$  as well.

Zone 1					Zone 2					Zone 3				
$qv_1$	$\times$	$\mathbf{B}_1$	=	$\mathbf{F}_1$	$qv_2$	$\times$	$\mathbf{B}_2$	=	$\mathbf{F}_2$	$qv_1$	$\times$	$\mathbf{B}_3$	=	$\mathbf{F}_3$
$\rightarrow$	$\times$	$\downarrow$	=	$\odot$	$\odot$	$\times$	$\rightarrow$	=	$\downarrow$	$\rightarrow$	$\times$	$\uparrow$	=	$\otimes$

Figure 36. Cross-products of velocity and B-field vectors by zone.

In Zone 1, the electron has a velocity from left to right across the page, and the perpendicular component of the B-field has a downward direction. The resulting force (calculated using the cross product and negating due to charge  $q$  as shown in Figure 36) on the electron would be out of the page. This force will give the electron a new velocity component  $\mathbf{v}_2$  directed out of the page. This velocity will cause the electron path to “spiral” as it heads into Zone 2.

In Zone 2, the electron has a velocity component  $\mathbf{v}_2$  directed out of the page. The perpendicular component of the B-field points left to right in this zone. The resulting force due to the interaction of  $\mathbf{v}_2$  and  $\mathbf{B}_2$  would be downward. This force will give the electron a new velocity component that will cause the beam to converge as it passed through the lens. The electron still has a velocity component  $\mathbf{v}_2$  that is causing it to spiral, and this component will be counteracted as we follow the electron into Zone 3.

In Zone 3, the electron has a velocity from left to right across the page, and the perpendicular component of the B-field has an upward direction. The resulting force on the electron would be into the page. This force will give the electron a new velocity component  $\mathbf{v}_3$  directed into the page. This new velocity component will cancel out the  $\mathbf{v}_3$  component from Zone 1 and “un-spiral” the electron beam. The spiraling component of the velocity causes the electrons to travel in a helical path (see Figure 37). It is important to note that while the exiting electrons no longer have a spiraling velocity component, they have been rotated with respect to their original position and also with respect to their position at the time of interaction with the sample. This usually does not matter, but must be taken into account when determining orientation of features on a sample.

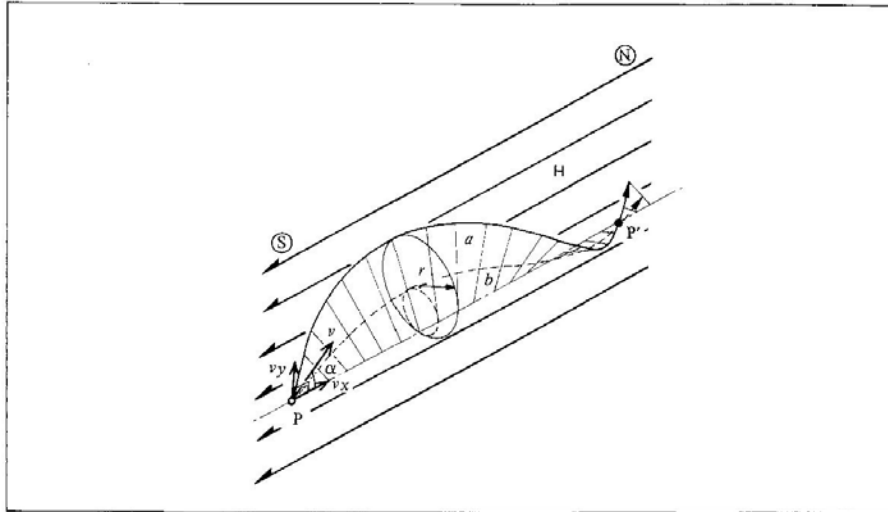


Figure 37. An electron starting at point P with velocity  $v$  will follow a helical trajectory in uniform magnetic field  $\vec{H}$ . The velocity component parallel to  $\vec{H}$ ,  $v_x$ , is uniform from P to P'. The velocity component that is perpendicular to  $\vec{H}$ ,  $v_y$ , causes the force that gives the circular motion to the helix. Taken from [25].

The JEOL 100CX has four electromagnetic lenses. The condenser lens, the objective lens, and the intermediate lens all have two solenoid coils and one pole piece and aperture. The projector lens has one solenoid coil and one pole piece and aperture.

### 2.5.3 Detectors and other Sensors

After the electrons interact with the sample, they must be detected in some way before the interactions can be analyzed and characterized. Electrons are detected using cathodoluminescence (CL), semiconductor detectors, charge coupled devices (CCD), and scintillator-photomultipliers.

#### 2.5.3.1 Cathodoluminescence (CL)

Cathodoluminescence (CL) occurs when electrons hit a screen that converts their energy into visible light. The screen emits light of intensity proportional to the number of electrons falling on the screen (see Figure 38). Viewing screens commonly use ZnS because of its relatively long luminescent decay rate (on the order of  $\mu\text{s}$ ). The ZnS is modified slightly so that its wavelength is around 550nm. This

produces green light, which is in the middle of the visible spectrum and is easiest to view with the human eye.

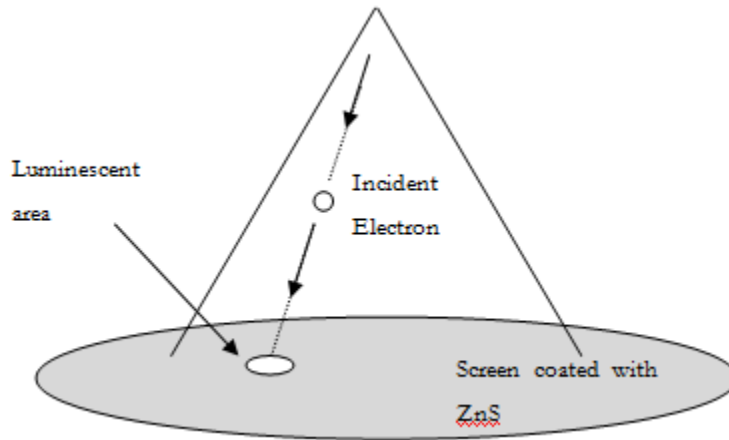


Figure 38. Cathodoluminescence occurs when electrons incident on the ZnS screen excite the ZnS and form a luminescent area for a time long enough to be viewed with the human eye or captured on camera.

### 2.5.3.2 Semiconductor detectors

Semiconductor detectors are made with some combination of Si and a thin metal film (Au or Al depending on the type) that form a 2 dimensional surface with p-n junctions (see Figure 39). Incoming electrons are converted to a current across the p-n junction, and this current readout is proportional to the number of electrons falling on the detector.

Semiconductor detectors are versatile and cheap to make. They can be formed into any flat shape and are often used for bright field and annular (ring-shaped) dark field detectors.

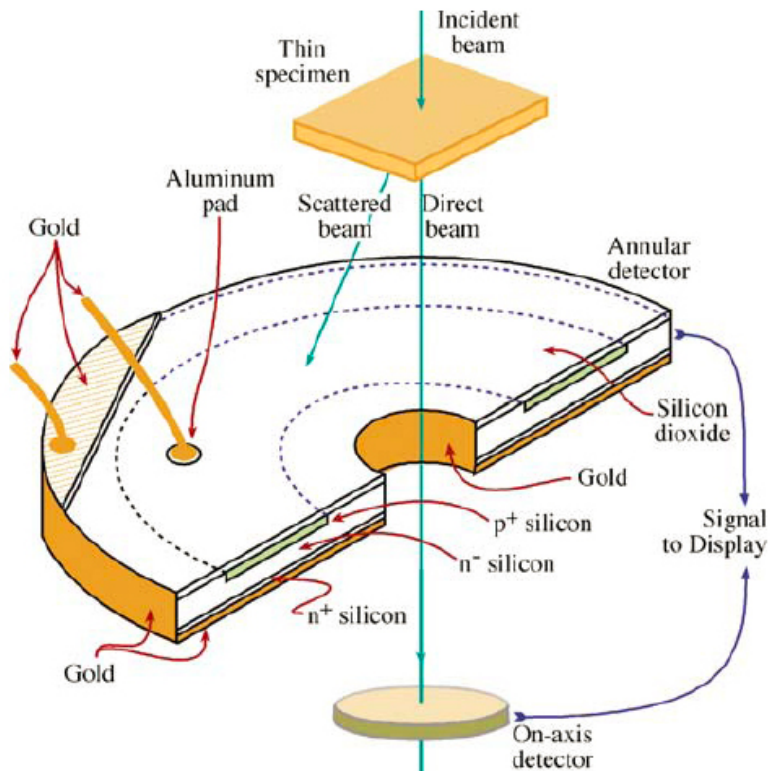


Figure 39. Cross section of a semiconductor detector made with layers of Si and Al. Au is used for the contacts and as a coating on the bottom and inner and outer edges.

Semiconductor detectors have inherently large capacitance and have a refresh rate of about 100kHz. They are not suitable for applications such as rapid STEM imaging. Semiconductor detectors also have a large dark current due to electron-hole pair thermal activation. This leads to a poor signal to noise ratio (DQE) for low intensity signals.

### 2.5.3.3 Charge Coupled Devices (CCD)

Charge Coupled Devices (CCDs) are pixel arrays consisting of thousands or millions of electrically isolated potential wells. Each pixel collects charge proportional to incident beam intensity. The charge collected in each cell is serially fed through an amplifier and digitized. The frame time to empty and refill is about 0.01s. Some CCDs read one column at a time, and some are designed to read multiple columns simultaneously (see Figure 40). Others are designed to transfer the analog signal to a

storage array, which is later digitized. Both designs allow for faster refresh times than the serial readout type.

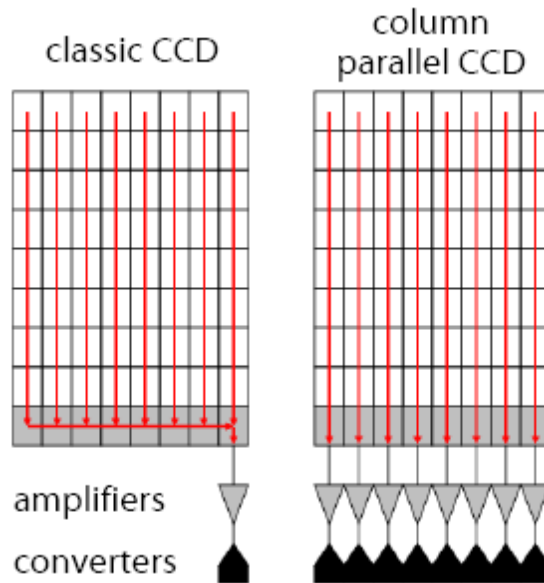


Figure 40. Classic CCD (left) vs column parallel CCD (right). Classic CCD transfers the signal from each pixel serially. Column parallel CCD transfers each column to an amplifier. Taken from [26].

CCDs work well for STEM applications because each pixel cell can correspond to a specimen area. They have good DQE ( $>0.5$ ), and therefore can be used for low intensity signals. They also have a high dynamic range for recording different intensities in diffraction patterns.

#### 2.5.3.4 Scintillator-Photomultipliers

The Scintillator-Photomultiplier is a detector that works better for low energy electrons. For this reason it is often used to detect secondary electrons. Electrons encounter a screen coated with a CL substance (the scintillator) and this screen gives off visible light. The light emitted is directed towards a photocathode which emits electrons into a photomultiplier tube to amplify the signal. The signal is amplified by a series of dynodes (see Figure 41). Each dynode is made of a material that emits secondary electrons. The number of electrons emitted from each dynode multiplies until the signal is

amplified by a factor of  $\sim 10^6$ . When the amplified signal reaches the cathode at the other end of the amplification tube, the signal is sent to a CRT to be viewed or captured.

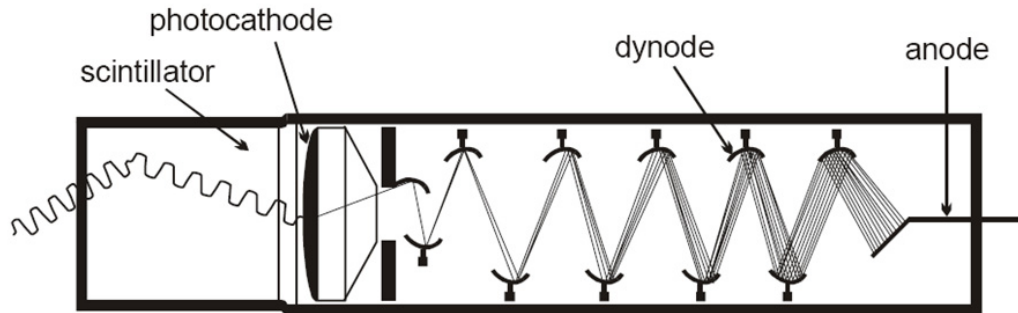


Figure 41. Scintillator-photomultiplier tube. The incoming electron wave is incident on the photocathode which is coated with photo-luminescent material. The series of dynodes in the photomultiplier (PM) tube amplify the photo-signal, and the anode picks up the amplified signal and sends it to the CRT or computer to be viewed and analyzed. Taken from [27].

Applications that need a longer delay time, such as viewing, use ZnS. Applications needing shorter delay periods, such as rapid scanning in STEM mode, use Ce-doped yttrium-aluminum garnet (YAG). YAG has a luminescent decay time on the order of nanoseconds and ZnS has a decay time on the order of microseconds.

Scintillator-Photomultiplier detectors have a high gain from PM tube, leading to a DQE of  $\sim 0.9$ . Their refresh rate is in the MHz range. This makes them more sensitive and faster than semiconductor detectors, though they tend to be more susceptible to radiation damage.

#### *2.5.4 Vacuum System*

Electrons are easily scattered by atoms, and therefore it is important to have an environment that does not interfere with the electron beam, with the exception of the specimen being observed. For this reason, electron microscopy is conducted in vacuum conditions. The JEOL TEM operates under high vacuum conditions in the range of  $10^{-6}$  Torr. The JEOL 100CX uses rotary vane mechanical pumps to achieve rough vacuum, and diffusion pumps to obtain and maintain high vacuum. These types will be

discussed further in sections 2.5.4.2-3. Other types of pumps that are sometimes used in TEMs are ion pumps, turbomolecular pumps, and cryogenic pumps.[1]

In order to achieve this low pressure, the sealed chamber is pumped in two stages. The first stage involves what are called rough pumps (or fore pumps). These pumps can pump high volumes of air, but do not reach pressures lower than  $\sim 10^{-3}$  Torr. This pressure range is considered rough vacuum pressure. Once rough vacuum is reached, high vacuum pumps take over to further lower the pressure.

High vacuum pumps have a lower pumping capacity than rough vacuum pumps. There are fewer air molecules in the system once the high vacuum pumps take over, so the pumping capacity doesn't need to be as great. High vacuum will be reached in a reasonable amount of time, and the rough vacuum pump can "back" the high vacuum pump – exhausting the air molecules as the high vacuum pump removes them from the system so that pressure doesn't build up behind the high vacuum pump and hinder its ability to obtain or maintain high vacuum conditions within the system.

The roughing and high vacuum pumps work together to attain and maintain the vacuum conditions needed for optimal TEM operation. They each have different methods of exhausting the molecules from the system, and they work together to maintain the flow of molecules from the vacuum area out into the atmosphere.

#### *2.5.4.1 Gas Flow and Throughput*

The way the gas molecules move or flow within the system is dependent upon the mean free path ( $\lambda_f$ ) at a given pressure and the size of the container or tubing. The mean free path is inversely proportional to the pressure. At lower pressures, there are fewer molecules per unit volume and they travel further on average between collisions.

The ratio between tube diameter ( $d$ ) and the MFP will determine whether the gas molecules are in viscous flow (like a liquid), molecular flow (each molecule acting independently), or somewhere in between.

$$\frac{d}{\lambda_f} > 1 \Rightarrow \text{viscous flow} \quad (34)$$

$$\frac{d}{\lambda_f} < 0.01 \Rightarrow \text{molecular flow} \quad (35)$$

$$0.01 < \frac{d}{\lambda_f} < 1 \Rightarrow \text{molecular flow} \quad (36)$$

Mechanical pumps only function in the viscous flow range. Diffusion pumps function into the molecular flow range.

The movement of the gas through the vacuum system is known as throughput. Throughput is the product of pump speed and pressure. The throughput is the same throughout a given system and depends on both the pump capacity and the physical geometry of the system (i.e. tube diameters, lengths, etc).[28]

#### 2.5.4.2 Roughing Pumps

Mechanical rotary pumps are capable of lowering the pressure to  $\sim 10^{-3}$  Torr. Many mechanical rotary pumps use oil as a lubricant for moving parts and as a medium to create air-tight seals between surfaces. Figure 42 shows a cross-sectional view of a mechanical rotary pump.

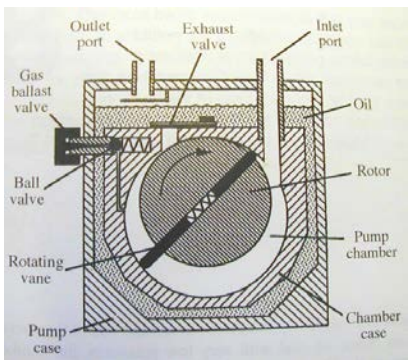


Figure 42. Mechanical Rotary Pump showing inlet, pump chamber, rotor and rotary vanes, ball valve, gas ballast valve, and outlet port. Taken from [1].

The mechanical rotary pump consists of a rotating cylinder that is offset in a larger cylindrical chamber. The rotating vane stays in contact with the outer cylindrical wall, creating a vacuum that

draws air in through the inlet port and then pushing the air through the exhaust valve, letting it escape into the atmosphere. A thin layer of oil coats the cylinder, vane, and chamber to make an airtight seal. The mechanical sequence that allows the rotary vane pump to create a vacuum is outlined in Figure 43.

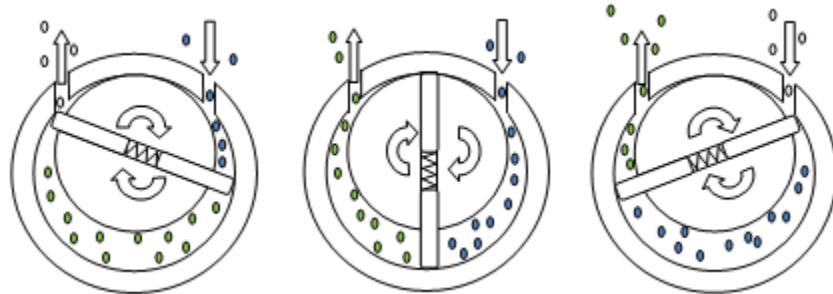


Figure 43. Rotary vane pumping sequence. From left to right: Step 1) Air is pulled into the inlet (blue) while previous intake volume is trapped between vanes and moving toward the exhaust port. Step 2) Air continues to be pulled in the intake (blue) while the previous volume is exhausted (green). Step 3) Intake volume is trapped between the vanes (blue) and is moved toward exhaust port.

### 2.5.4.3 Diffusion Pumps

Oil diffusion pumps (see Figure 44) use heated oil vapor and momentum transfer to remove gas molecules from the system and lower the pressure. They are used to obtain high vacuum conditions.

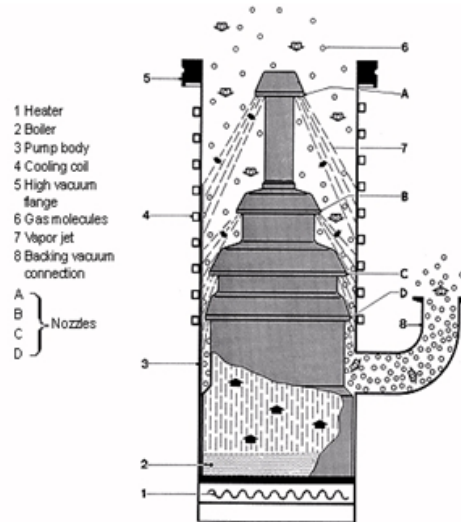


Figure 44. Diffusion Pump attached to the system with a high vacuum flange (5). The Heater (1) heats the oil in the boiler. The oil vapor formed (7) is directed downward at an angle toward the walls of the pump body (3) which are cooled by water cooling coils (4). The gas molecules (6) that encounter the high-velocity oil vapor (7) are knocked towards the walls where they condense and are directed downward with the returning cooled oil on the walls. The gas molecules are then exhausted through the backing vacuum connection (8). Taken from [1].

The oil vapor forms jets (3) and the high energy oil molecules in these jets transfer their momentum to free gas molecules, causing them to be trapped in the condensed oil on the walls of the pump. The gas molecules are then expelled through the backing vent (8) by a roughing pump.

Oil vapor from the diffusion pump sometimes backs into the vacuum chamber and contaminates the vacuum environment. Liquid N<sub>2</sub> traps are often used in order to minimize back-streaming of oil vapor.

## Chapter 3

### ANALYSIS AND MODIFICATIONS

#### 3.1 Instrument Overview

This section will give an overview of the vacuum system, electron gun, optics and image formation system, electronics, detection sensors, and sample chamber of the JEOL 100CX TEM. The main column of the instrument is shown below in Figure 45.

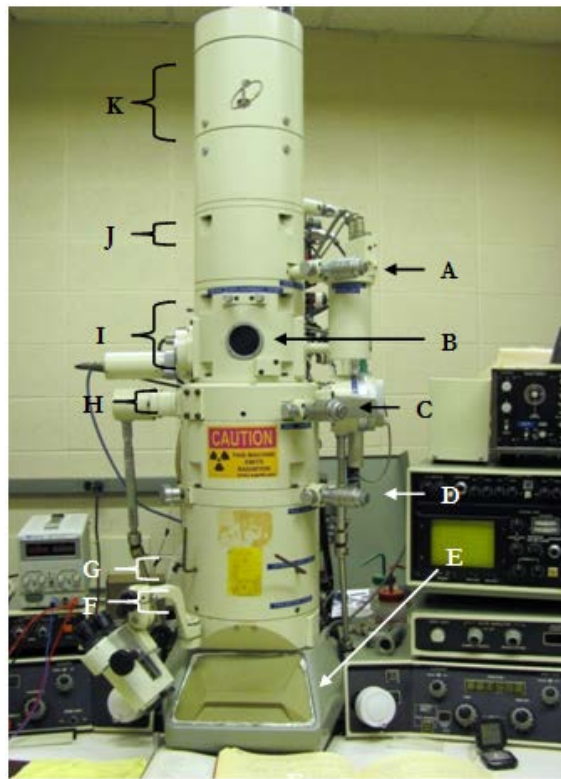


Figure 45. JEOL 100CX main column. The electron beam originates in the anode chamber (K), passes through the condenser lens (J) and condenser lens aperture (A), interacts with the specimen in the specimen chamber (I), passes through the objective lens (H) and objective lens aperture (C), then through the field limiting aperture (D), through the intermediate lens (G) and the projector lens (F), and terminates in the viewing chamber (E) where it is converted into a signal or image that can be analyzed.

### *3.1.1 Vacuum System*

The vacuum system is designed for ease of use and has an ultimate pressure of  $\sim 1 \times 10^{-6}$  Torr. When each part is operating correctly and there are no leaks, the system can be started and then left to run until operating conditions for the electron beam are obtained. Three Pirani type gauges are used to monitor the pressure in the system. They are located in the anode chamber, column, camera chamber. These gauges feed pressure readings back to the automated control system in order to determine the correct valve open/close sequence. Figure 46 shows a schematic of the 100CX vacuum system.

#### *3.1.1.1 Pumpdown Sequence*

The column, the anode chamber, and the camera chamber are evacuated in that order. The pressure in respective chambers can be monitored on the VACUUM GAUGE meter. The Diffusion Pumps (DPs) and the desiccator are pumped down before the main column. Valves 11, 14, and 24 are open during this step.

When the pressure in the Diffusion Pumps is low enough, Valves 11, 14, and 24 close, shutting the Diffusion Pumps off from the Rotary Pumps. After this, Diffusion Pump heaters are turned on. Valves 25, 10, and 26 open and the column is then pumped to rough vacuum by the Rotary Pumps.

The vacuum reservoir between the Diffusion Pump and the Rotary Pump acts as a holding tank for gases and the Rotary Pump will empty the reservoir when it is full. Valve 11 will open as needed to allow rotary pump 1 to back the diffusion pumps.

Valve 10 closes when the main column reaches rough vacuum. Valve 25 may stay open so that the camera chamber and the anode chamber can be pumped to rough vacuum. Valves 7 and 8 open the DP's to the chamber to reduce the pressure further to high vacuum.

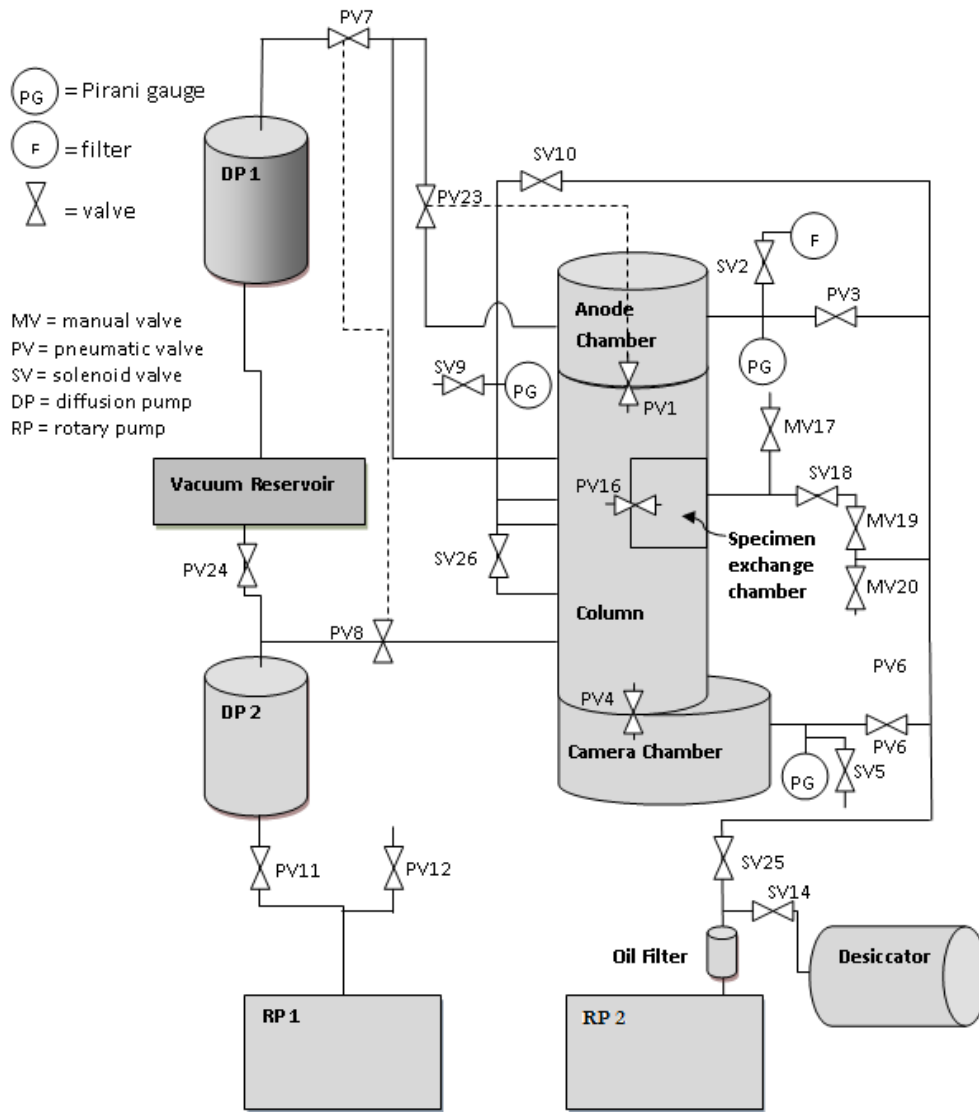


Figure 46. JEOL 100CX vacuum system. The solid lines represent vacuum connections (tubes or direct connections). The dotted lines connecting PV7 to PV8, and PV1 to PV23 mean that they have the same open/close trigger and operate simultaneously. See Pneumatic System diagram in Appendix D: Additional Diagrams and Schematics.

Once the vacuum system reaches high vacuum, the diffusion pumps continue to run to maintain high vacuum conditions. At this point, the rotary pumps are only used to back the diffusion pumps as needed or to pump down specific sections of the TEM when they need to be opened to atmosphere as a part of regular operation or maintenance. The specimen chamber, the anode chamber, the camera chamber, and the desiccators are all designed so that they can be isolated, exposed to atmosphere, and pumped down again relatively easily.

#### *3.1.1.2 Rotary Vane Pumps*

The JEOL 100CX uses two rotary vane roughing pumps to bring the pressure in the system from atmosphere to  $\sim 10^{-3}$  Torr. These pumps can pump efficiently as long as the gas flow is in viscous or turbulent flow. The pumping capacity of each rotary vane pump is  $\sim 75$  L/min. Below around 100 mTorr, the flow begins to transition to molecular (each molecule travels independently due to the increase of the mean free path at lower gas densities)[29]. At this point, the probability of oil molecules backstreaming into the system increases. One way to address this issue is to use a trap to limit backstreaming. Rotary pump 2 has a molecular sieve trap for this purpose. This pressure range is at the high end of the diffusion pump operation range, and the diffusion pumps can be employed at this point in order to prevent rotary pump backstreaming.

Rotary vane pumps require little maintenance and can efficiently pump high volumes of air at higher pressures. This makes them a good choice both for pumping down chambers that routinely are opened to atmospheric pressure (specimen chamber, desiccators, and camera chambers) and for backing diffusion pumps that may produce relatively high pressures at the exhaust port connected to the roughing pump when they are first turned on in the mTorr range.

#### *3.1.1.3 Diffusion Pumps*

Diffusion pumps are used in the JEOL 100CX to obtain and maintain high vacuum pressures in the  $10^{-6}$  Torr range and have a pumping capacity of  $\sim 400$  L/sec. Diffusion pumps are a good choice specifically for a TEM for two reasons. The first is that they have no moving parts and therefore do not cause vibrations that would interfere with the stability of the image. The second is that they have a large pumping capacity compared with other high vacuum pumps. This minimizes the time required

to pump out air from the specimen chamber, camera chamber, or any other chamber that might need to be accessed and opened to atmosphere during regular operation or maintenance. In addition, diffusion pumps require very little maintenance and are very reliable.

One potential negative concerning diffusion pumps is the possibility of oil contamination. The pump is designed to direct the flow of oil molecules away from the vacuum system so that they are contained within the pump. When used and maintained properly, possibility of contamination is minimized. Liquid nitrogen cooled baffles can be used to further reduce oil contamination.

### 3.1.1.4 Pirani Gauges

The Pirani Gauges used in the 100CX have a range of sensitivity from atmospheric pressure down through the range of  $\sim 1 \times 10^{-6}$  Torr required for TEM operation. They are used to sense vacuum pressure and automate the pumping process. A schematic of the Pirani Gauge can be seen in Figure 47.

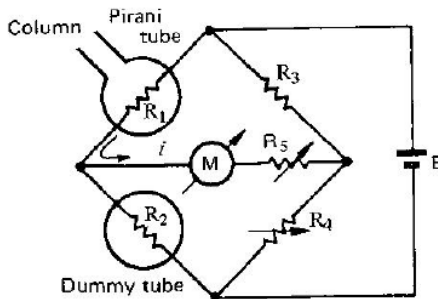


Figure 47. A Pirani gauge circuit. The dummy tube and Pirani tube resistors are identical except for the difference in pressure. The dummy tube is sealed and is kept at a constant pressure of  $\sim 10^{-5}$  Torr.[30] The difference in resistance leads to a current through ammeter M. This current signal leads to a pressure reading.

A Pirani gauge is based on the principle that the temperature of a resistor will be affected by the heat conductivity of the gas that surrounds it. If the pressure goes up, more heat can be conducted and the

resistor cools slightly. If the pressure decreases, the resistor remains at a higher temperature. A higher temperature will increase the resistance.

### 3.1.2 Electron Gun

The electron gun used in the JEOL100CX is a thermionic emission gun as outlined in section 2.5.1.3. The filament is a tungsten pre-centered hairpin type with DC heating. Figure 48 shows the schematic of the electron gun and the contours of the equipotential lines through the potential difference between the cathode (filament), Wehnelt (grid), and the anode.

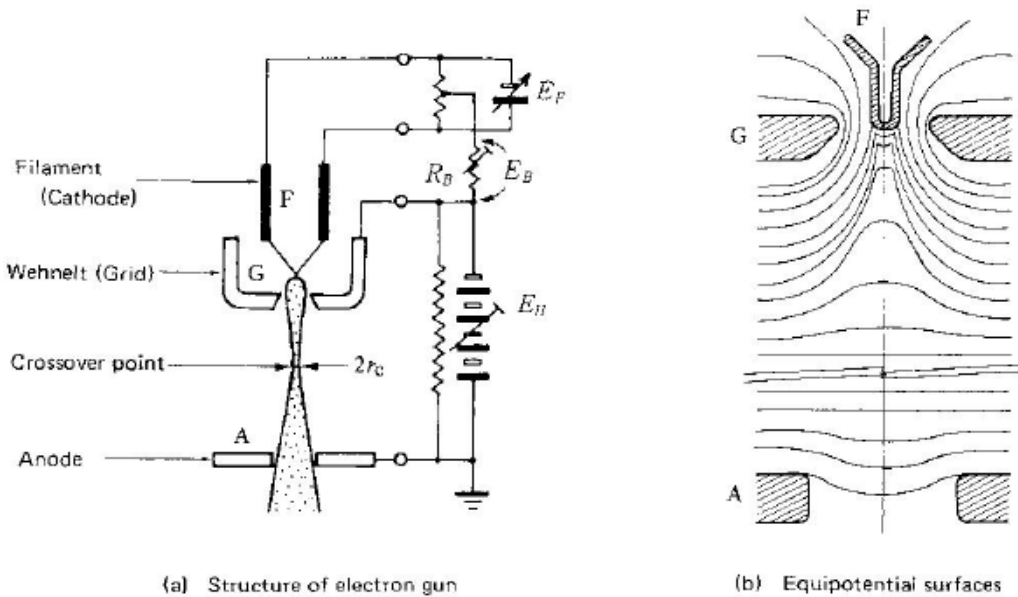


Figure 48. JEOL 100CX self-biasing electron gun. The electron gun is composed of a negatively biased cathode filament (F) and Wehnelt cylinder (grid, G), and an anode plate (A) with a hole in the center at ground potential. The potential drop between the filament and anode is the accelerating potential, while the filament current which floats at the cathode potential has its own control. The source characteristics are determined by the position, shape, and electromagnetic properties of the F, G, and A. The equipotential surfaces in (b) show lower potential around the centerline of the electron path.

### 3.1.3 Optics and Image Formation

#### 3.1.3.1 Lenses and Apertures

The 100CX has a pre-specimen condenser lens, an objective lens, 1<sup>st</sup> and 2<sup>nd</sup> intermediate lenses, and a projector lens (see Figure 49). The condenser lens determines how the electron beam interacts with the specimen. The condenser lens aperture, objective lens aperture, and the field limiting aperture can all be used to control the size of the electron beam. The post-specimen lenses are considered part of the image formation system. Beam deflection coils and scanning coils (used in STEM) are also used in some imaging applications.

Figure 50 shows a ray diagram of selected area (SA) diffraction versus SA imaging. The combination of lenses and apertures that are used for imaging applications and selected area (SA) diffraction patterns in more detail in 2.4 Imaging and Analysis Techniques based on Electron Scattering. Figure 51 shows the physical placement of the lenses in the main column of the 100CX.

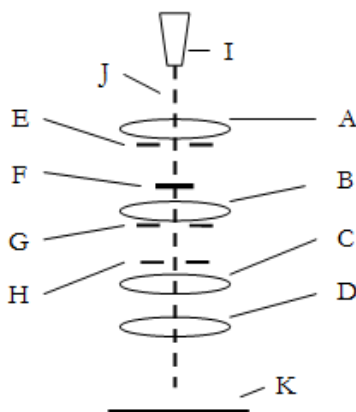


Figure 49. Optical system of JEOL100CX. The electron gun (I) produces a beam of electrons (J) that passes through a series of lenses and apertures. The condenser lens (A) and condenser lens aperture (E) focus and limit the beam before it interacts with the sample (F). The beam then passes through objective lens (B) and aperture (G), the field limiting aperture (H), the intermediate lens(es) (C), and the projector lens (D) before encountering the viewing screen (K).

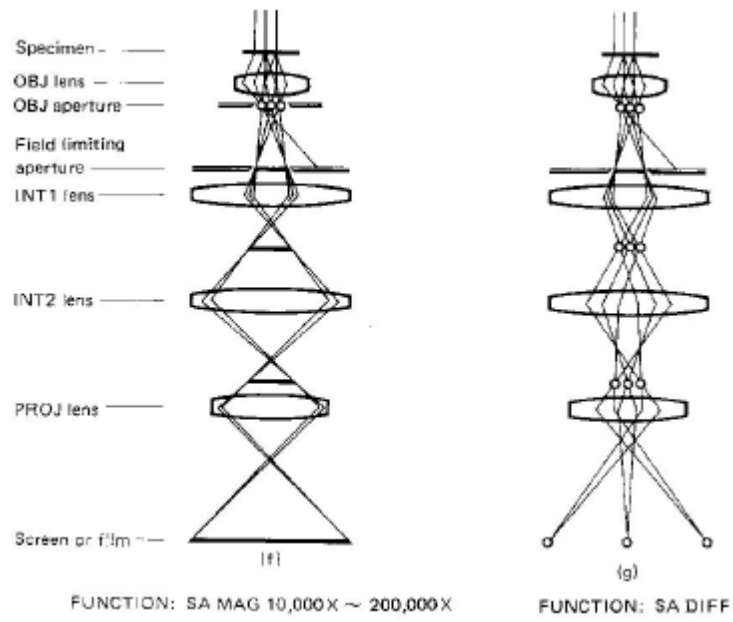


Figure 50. Selected Area (SA) image versus SA diffraction. Selected area magnification (f) requires that one or more diffraction spots are selected using the OBJ aperture to form an image. Selected area diffraction (g) uses a parallel beam incident on the specimen and projects the diffraction pattern as an image.

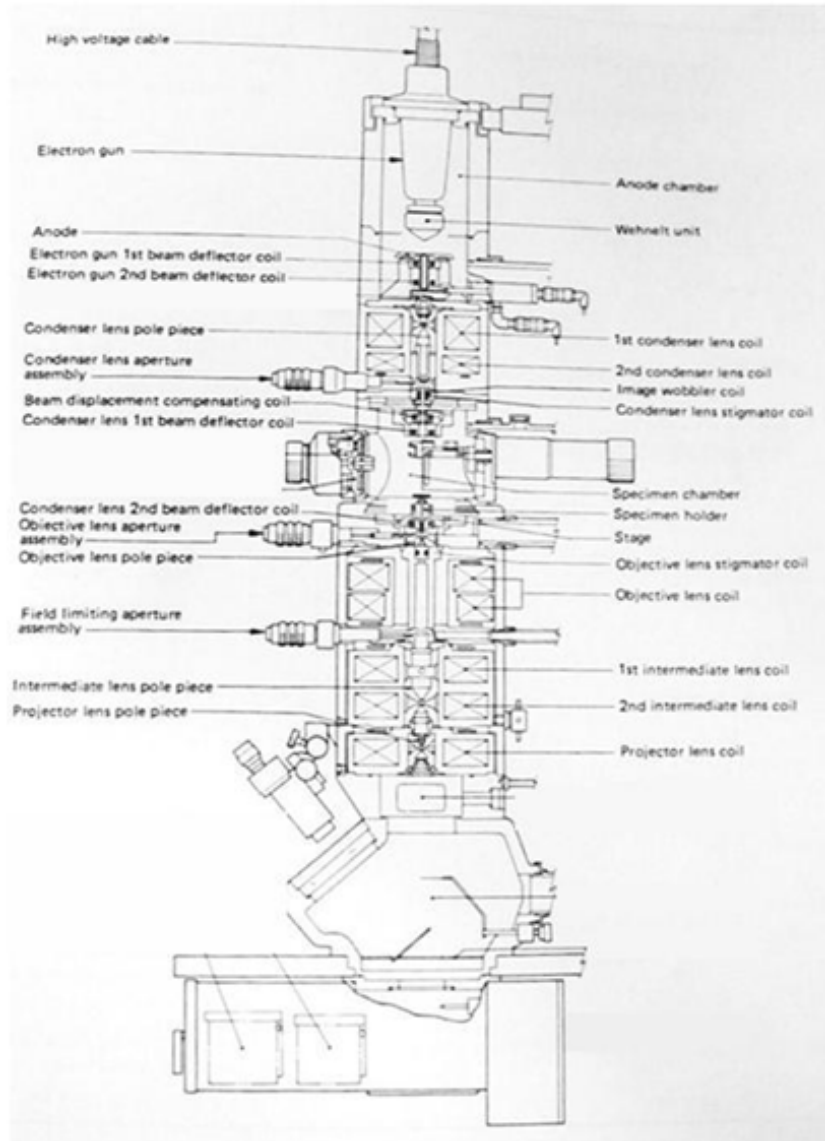


Figure 51. Main column cutaway view showing placement of lenses, pole pieces, apertures, and deflection coils. The electron gun deflector coils are used to align the electron beam. The condenser lens beam deflector coils are used to scan the beam in the x and y-directions during STEM operation.

### *3.1.3.2 Beam Deflection Coils*

In order to manipulate the placement of the electron beam for alignment, a set of deflection coils located before the condenser lenses is used. Another set of deflection coils called the scanning coils are located between the condenser lens and the sample and are used to scan the beam across the sample during STEM mode. See Figure 51 for location of condenser lens beam deflector coils.

### *3.1.3.3 Bright Field/Dark Field (BF/DF) Coil Unit*

The BF/DF coil is located inside the objective lens and is used to switch between BF and DF images. When current is flowing through the BF/DF coil, the electromagnetic field deflects the electron beam off axis so that a less intense diffracted beam passes through the field limiting aperture rather than the brighter transmitted electron beam (see Figure 52). Selecting the transmitted beam with the field-limiting aperture will form a bright field image. Deflecting the beam with the BF/DF coil and selecting a diffracted beam will form a dark field image. The BF/DF coil unit is composed of four solenoid coils oriented orthogonally (see Figure 53). There are two sets of opposite coils each controlling x-axis and y-axis deflection, respectively.

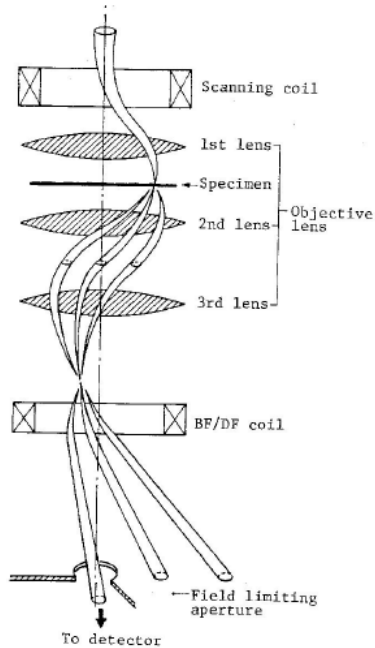


Figure 52. BF/DF coil unit. Deflector coils shift the electron beam to select the bright on-axis beam or the less intense diffracted beam to form a BF or DF image, respectively. The scanning coils above the specimen determine which area of the specimen is going to be imaged. The 1<sup>st</sup> lens focuses the incident electron beam on the specimen surface, the 2<sup>nd</sup> lens forms a diffraction pattern in the image plane, and the 3<sup>rd</sup> lens projects the diffraction pattern onto the field limiting aperture plane.

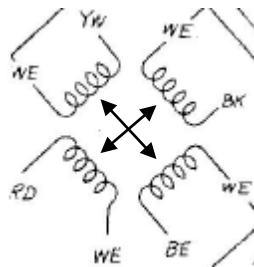


Figure 53. BF/DF coil consists of two sets of solenoid coils. Each set can shift the beam along one axis.

#### *3.1.3.4 Specifications*

The resolution capability for the JEOL 100CX is 1.4Å for lattice resolution and 3Å for point to point resolution. Lattice resolution is the minimum distance between lattice planes that produces a distinct diffraction pattern. Point-to-point resolution is the minimum separation distance of electron-sample interaction that will resolve as two distinct points in the density contrast image. The minimum beam spot size is 0.3µm in diameter on the specimen.

#### *3.1.4 Electronics*

The electrical system of the 100CX consists of four main parts: a high voltage power supply (electron beam acceleration), an EM lens power supply, a deflector coil power supply, and various other control circuits (vacuum system, camera system, electron gun filament, etc.).

The majority of the circuits in the TEM need to be relatively stable as they control sensitive components such as lens current, beam current, or deflector coil current. A small variation in these sensitive circuits would dramatically hinder the ability to form a stable image.

##### *3.1.4.1 High Voltage Power Supply Circuit*

The high voltage oscillator circuit (Figure 54) produces a sinusoidal wave with stable amplitude in order to supply steady power, while the rectifying circuit converts to DC in order to generate a stable electron beam. The accelerating voltage ranges from 20 to 100 kV and can be set at intermediate values in increments of 20 kV.

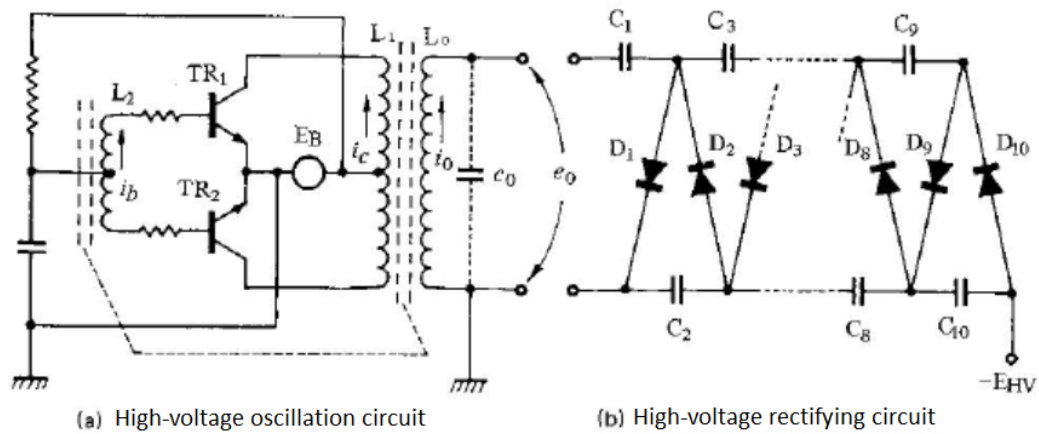


Figure 54. High voltage power supply showing HV oscillation circuit (a) and HV rectifying circuit (b). The oscillation circuit provides a stable sinusoidal wave, which is converted to DC and amplified by the rectifying circuit.

### 3.1.4.2 Lens and Deflector Current Supply Circuits

The circuits for the lenses and deflector coils must have highly stabilized current. Self-stabilizing constant-current circuits (Figure 55) are used to maintain this stability.

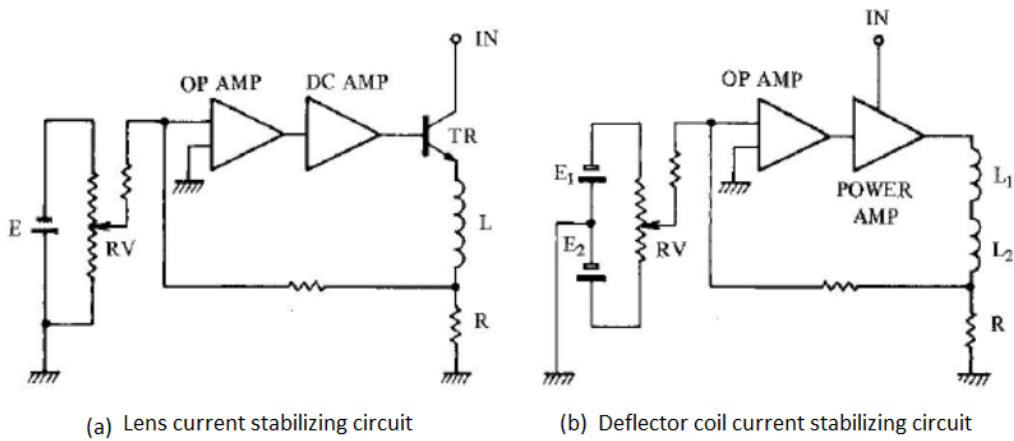


Figure 55. Lens (a) and deflector coil (b) current stabilization circuits.

Any variation in the current through the lens or deflector coils is detected as a change in voltage at the reference resistor R. This voltage is compared to the supply voltage ( $E, E_1, E_2$ ) through the feedback loop. Any variation is rectified and stabilized by the OP AMP and DC or POWER AMP in the feedback loop. The load current is adjusted by the variable resistor (RV).

### 3.1.4.3 Electronic Systems Flowchart

A general outline of how the power input for the 100CX TEM is broken up into different circuits is found in Figure 56.

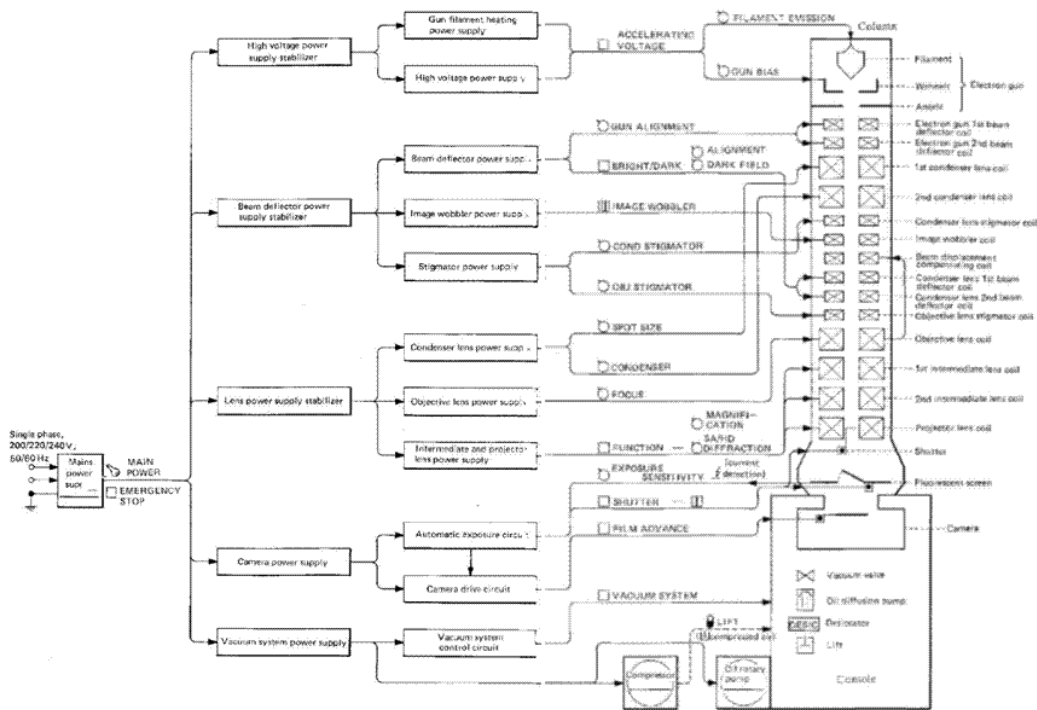


Figure 56. JEOL 100CX Electrical systems flowchart. The HV power supply, beam deflector coils, lens power supply, camera system, and vacuum system circuits are shown.

### 3.1.5 Sensors

The 100CX TEM is equipped with multiple sensors for detecting electrons. These include a photo-luminescent viewing screen, a photographic emulsion film camera, a backscattered electron detector (BSE), and an EM-ASD Scanning Diffraction Device that uses a photomultiplier tube (PMT) to detect the electron signal in diffraction mode.

#### 3.1.5.1 Phosphor Viewing Screen

The 100CX has a phosphor viewing screen in the viewing chamber (see Figure 57). The projector lens projects the final image on the photo-luminescent material. The screen can be viewed with or without the binoculars through the viewing window. The electrons cause the photo luminescent material on the screen to fluoresce and the image formed can be viewed with the human eye. See section 2.5.3.1 Cathodoluminescence (CL) for further explanation.

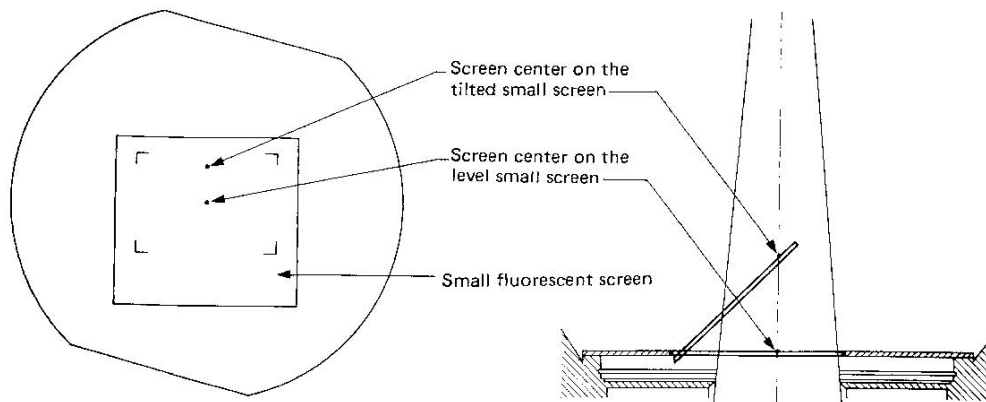


Figure 57. The phosphor viewing screen can lay flat, can be tilted 45° for viewing, and can be tilted 90° to allow the electron beam to be transmitted to the camera chamber below.

### *3.1.5.2 Film Camera*

The 100CX has a film camera located in a chamber just below the viewing chamber (see Figure 58). The electrons that form the image are transmitted to the electron-sensitive film for a predetermined exposure time. The film chamber can be isolated from the rest of the system and opened to access the film for processing (see Figure 59).

Electron sensitive film is known as a photographic emulsion. Photographic emulsions are suspensions of silver halide grains in a gel. When electrons strike the halide, they ionize it and transform it into silver. Films can be manufactured as polymer films or glass plates and have a range of film speeds just like camera film. In general, the higher speed film has larger grain size and lower resolution. In practice, TEM images are most often formed using fast film and low exposure time.

Film has a low dynamic range and degrades the vacuum within the TEM. The polymer stands and the film itself both outgas hydrocarbons and water vapor. CCDs have an advantage over film in both of these areas[1] (see 2.5.3.3 Charge Coupled Devices (CCD)).

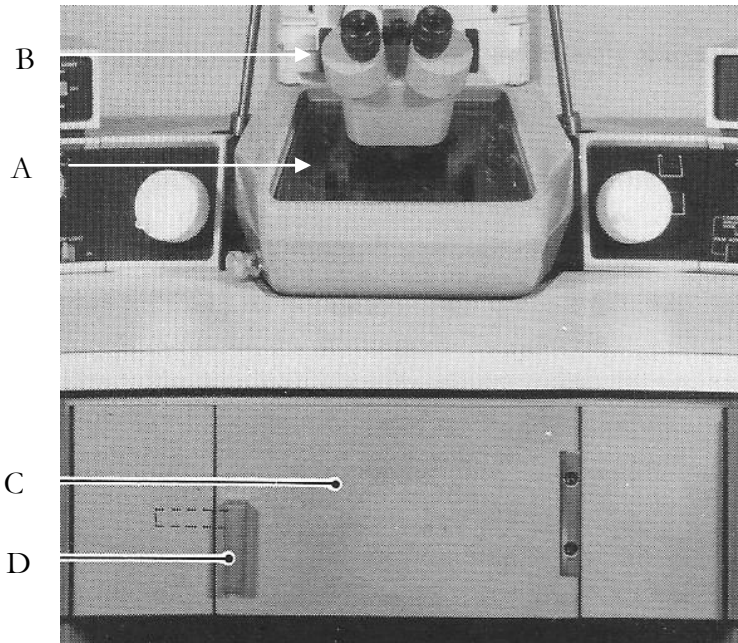


Figure 58. Viewing chamber (A) and camera chamber (C). Removable binoculars (B) may be used when viewing the phosphor screen. The camera chamber can be opened to change or process film using the airlock lever (D).

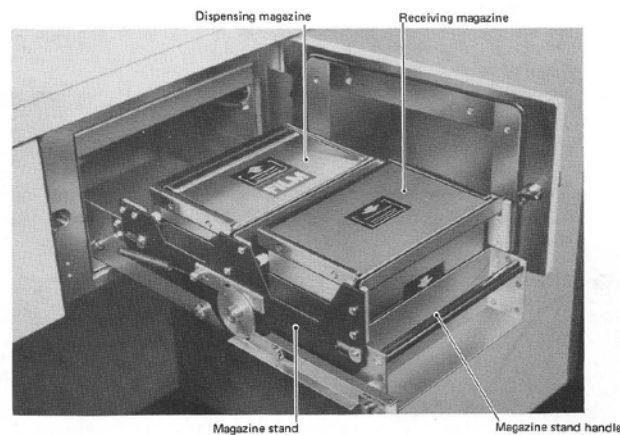


Figure 59. Open camera chamber. The magazines can be removed or exchanged while the chamber is open.

### 3.1.5.3 Backscattered Electron Detector (BSE)

The STEM system of the 100CX is equipped with a backscattered electron detector (BSE). This detector provides compositional and topographical information when the microscope is in STEM mode. The sensor consists of two electron sensors mounted on opposite sides of the electron beam at opposite angles with respect to the specimen. The number of backscattered electrons (BSEs) that fall on each detector depends on the composition of the sample and the topography. A material with a higher  $z$ -value will have higher numbers of BSEs. The geometry of the surface also affects the number and trajectory of BSEs, as seen in Figure 60. The composition image signal is constructed by adding the signals from each detector. The topographic signal is constructed by subtracting the signals from each detector. Figure 61 shows detector geometry and signal composition.

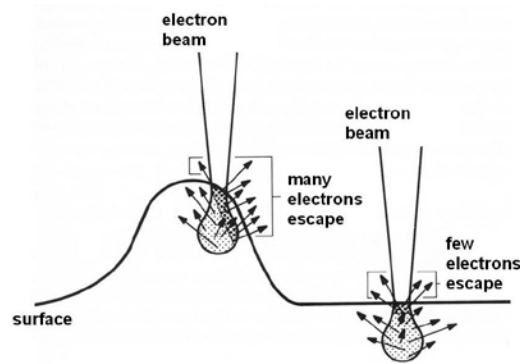


Figure 60. The number of BSEs is affected by surface topography. Edges and points emit more BSEs and flat areas or depressions emit fewer. Taken from [31].

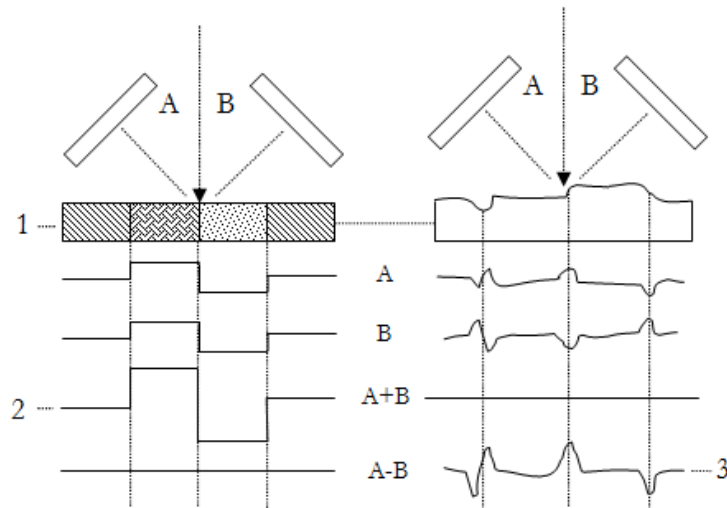


Figure 61. An electron beam incident on a sample surface (1) of uniform composition will produce a relatively constant number of BSEs. A beam incident on a slanted surface will emit more BSEs and will direct a stronger signal toward the detector whose orientation is closer to parallel with the surface of the sample at that point. The added signals from detectors A and B (2) provide a composition signal, and the difference of A and B (3) provides topographical slope, which can be used to construct a topographical map of the surface.

#### 3.1.5.4 EM-ASD Scanning Diffraction Device

The EM-ASD Scanning Diffraction Device (Figure 62) is used to display and record a two dimensional diffraction pattern. This device allows both the spatial orientation and the intensity distribution of the pattern to be recorded for analysis. The diffraction pattern is two dimensionally scanned using the ASD deflection coils mounted just beneath the projector lens. The x-axis is scanned analogically, and the y-axis digitally (16, 32, 64, 128, or 256 steps). The electrons that pass through the ASD aperture (located beneath the camera box) enter a photomultiplier tube (PMT). The signal from the PMT controls the y-axis of a CRT which is synchronized with the ASD coils, constructing an image that is analogous to the 2-dimensional scanned surface.

The PMT has the advantage of allowing detection over a wide range of intensity. A logarithmic amplifier allows a wider range of intensities to be included on the same screen because the upper values are condensed.

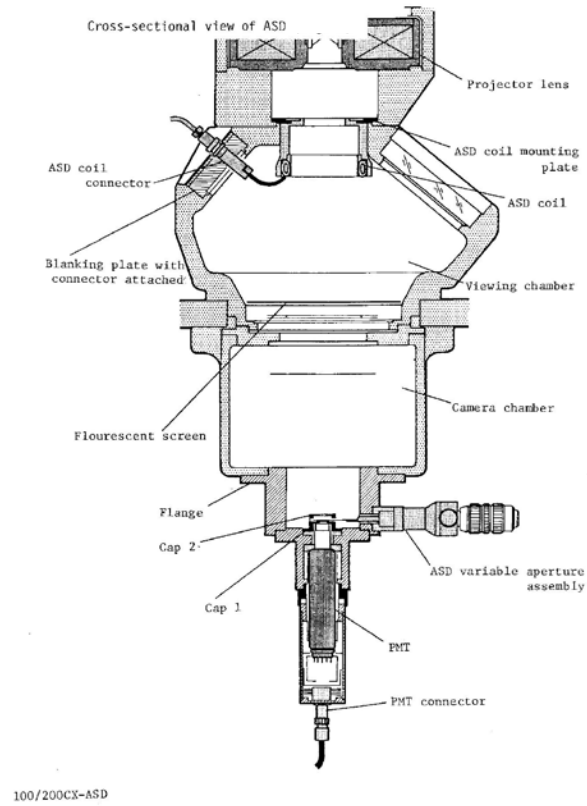


Figure 62. Cross sectional view of ASD system. ASD scanning coil mounted directly below the projector lens, ASD variable aperture assembly to control the diameter of the beam entering the Photomultiplier Tube (PMT), and the PMT and connector are shown. The ASD scanning coils manipulate the diffraction image in the x-y plane so that the relative intensities can be picked up by the PMT and compose an intensity map of the diffraction pattern.

### 3.1.6 Sample Chamber and Holder

The sample chamber includes an airlock mechanism with anti-contamination device (liquid nitrogen baffle). The sample holder has capacity for 6 specimens and the sample movement range is  $\pm 1$  mm.

The JEOL 100CX is equipped with a side entry goniometer (SEG). See Table 1 for SEG specifications. Two specimens can be mounted in the holder at once, and the specimen selector is used to change between specimens. Various types of specimen holders (outlined in Appendix C: Specimen Holders) are available for use with the goniometer depending on application.

The tilting and rotating holders are particularly useful in electron diffraction. The crystal lattice must form a small enough angle with respect to the incident electron beam in order for Bragg diffraction to occur. The SEG allows the specimen to be tilted along the x-axis, and the addition of a tilting specimen holder allows the specimen to be tilted along the y-axis as well. The use of a rotating holder (Figure 63) allows for multiple lattice planes to be imaged by changing the orientation of the specimen with respect to the tilt axis of the SEG and therefore allowing multiple orientations to be explored and imaged. The x-axis and y-axis tilt functions are controlled with the pedal switches on the floor under the main column (Figure 64). The tilt speed is controlled using the x-tilt and y-tilt knobs on control panel A.

Table 1 SEG specifications

	Angle (degrees)	Speed (degrees/min)
x-tilt	$\pm 60$	9 – 90
y-tilt (with tilting holder)	$\pm 45$	5-50
Rotation (with rotating holder)	$\pm 360$	12-120

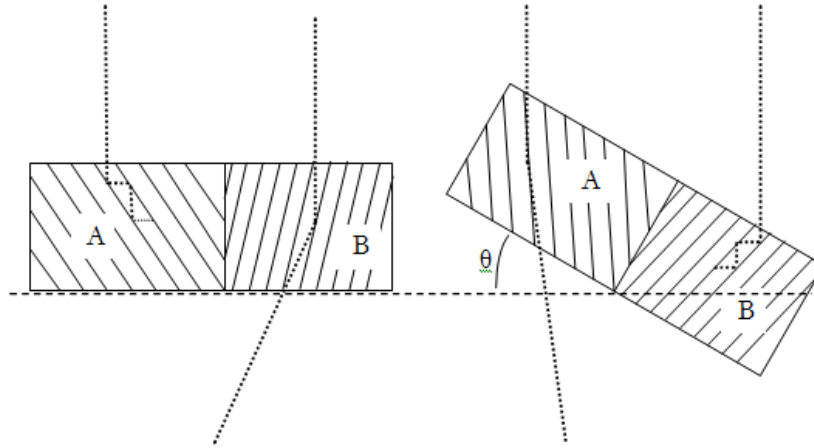


Figure 63. Effect of tilting a specimen in diffraction mode. In a specimen with lattice orientations A and B, an electron beam incident on B will diffract strongly while a beam incident on A at the same angle will not diffract well because of the high angle of incidence with respect to the lattice plane. If the sample is tilted an angle  $\theta = 30^\circ$  in the clockwise direction, the situation reverses and orientation A diffracts strongly while B does not diffract.

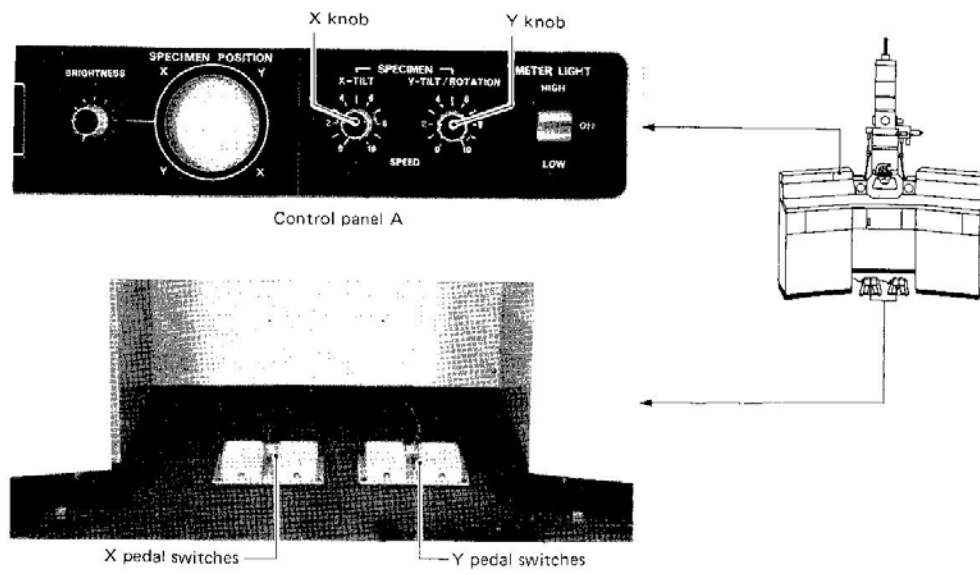


Figure 64. X and Y tilt speed control knobs and tilt control pedals. The y knob for speed control is used to control rotation speed when the rotating holder is in use.

### 3.2 Modifications

As a first step toward restoring full operation of the JEOL 100CX TEM, the vacuum system was analyzed and some modifications were made in order to fix problems and pinpoint trouble areas. The results of any investigations or modifications that have been made to the system are here explained.

#### 3.2.1 Disassembly and Repair of Rotary Vane Pump #2 (RP2)

Early on in the project, rotary vane pump #1 (RP1) was running, but rotary vane pump 2(RP2) was not running. Rotary Pump2 was disassembled and cleaned. It was found that the springs holding the rotating vane flush to the outside of the vacuum chamber had lost their elasticity. The space in the holes was partially filled in with sheared bolts so the vanes would push with greater force against the outside walls of the pumping chamber (see Figure 65). Upon reassembly, Rotary Pump 2 still did not work.

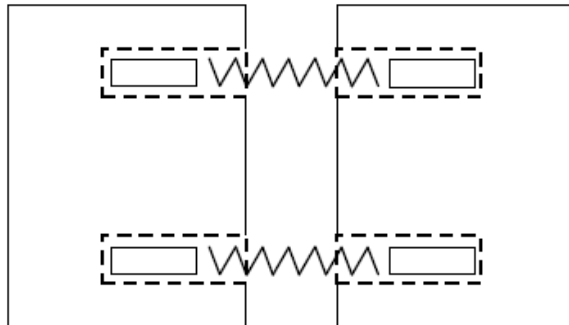


Figure 65. Two-sided vane removed from the rotating drum. The sheared bolts are represented by the four rectangular blocks at either end of the two springs.

The rotary pumps are run by a belt connected to an electric motor. After RP2 failed to work properly when reassembled, the electric motors on RP1 and RP2 were switched as a test to determine whether the problem was due to a bad motor or bad electric circuit. After the switch, both pumps worked. The reason was unclear, but at this point both pumps were functional and the troubleshooting process could move toward other areas of the vacuum system.

### *3.2.2 Oil Filter Restoration*

RP2 is connected to a cylindrical oil vapor filter, and then to the rest of the system. This filter is full of molecular sieve pellets that “absorb” stray oil molecules so that they do not make their way into the rest of the system. When the pellets are saturated, they will no longer do their job of preventing contamination, and may actually become a source of contamination and outgas, making the pressure in the system higher. It was found that there was a pressure increase of almost an order of magnitude across this oil filter ( $1.0 \cdot 10^{-2}$  Torr on the pump side and  $9.0 \cdot 10^{-2}$  Torr on the vacuum side). The filter was emptied, and the pellets were baked under vacuum with a partial pressure of inert gas to purge the evaporated oil molecules. (see A.2 Molecular Sieve for bake parameters).

### *3.2.3 Conversion of Valve Control System to Manual Operation*

In order to isolate each section and each valve of the vacuum system, it was decided that some of the valves should be converted to manual control. Valves 10, 25, and 26 were initially chosen because they were the ones that connected the column chamber to Rotary Pump2.

The wires supplying power to the solenoids of valves 10, 25, and 26 were removed and clearly labeled (valve number and +/-). The valves were then connected to a DC power supply as shown in Figure 66.

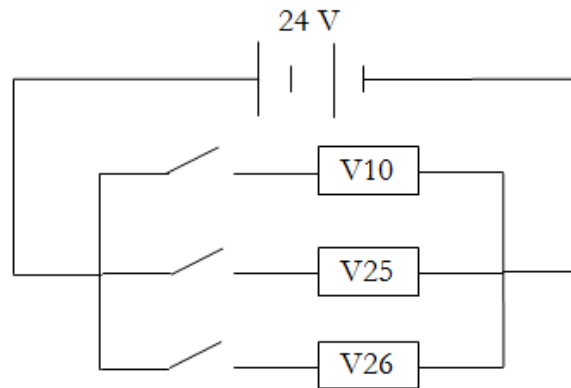


Figure 66. Manual valve control schematic. Valves 10, 25, and 26 were disconnected from the automatic controls and connected in parallel to a 24 Volt DC power supply. Each valve has its own manual switch.

It is important to note that this setup should only be temporary and that precautions must be taken while part of the system is automatic and part is manually controlled (See caution in A.1 Manual/Automatic Transfer Switch). Valves 7 and 8 were later converted to manual control, thereby reducing the risk of backstreaming contamination.

A master switch to change between the automatic (default) and manual mode was installed. This switch has two input ports, A and B, each with 25 pins, and one output port, also with 25 pins. The switch either connects all the A pins to their respective output pins, or all the B pins to the output pins. This multiple circuit switch was wired so that the valve system could be easily toggled between Automatic (A) mode and Manual (B) mode. Each input has a positive power line and a ground line to correspond to each solenoid valve. The A input has two pins associated with each valve, one with power coming from the system computer and one returning to the system at a lower potential (possibly at ground potential, but not necessarily). The output has two lines dedicated to each valve – one with power output and the other to return to ground. Pin and valve associations are outlined in Appendix A: Modified Systems.

In the event that the rough vacuum of the main chamber reaches sufficient low pressure to allow the diffusion pumps to take over, the valve control can be switched from manual to automatic to ensure that the appropriate sequence of valve operation. There are some valves that are not included in the manual circuitry, and therefore it is safer to operate in the automatic mode once the troubleshooting is finished and the leaks are found and repaired.

### *3.2.4 Disassembly and Cleaning of Diffusion Pumps*

Incorrect operation of the diffusion pumps in the past could have caused contamination in the diffusion pump or in the column chamber.

When the diffusions pumps were removed and examined, a dark brown coating was found over much of the surface area of the oil vapor nozzles. Oil breakdown results from exceeding maximum foreline pressure. If the diffusion pump is not properly backed by the rotary pump, or if it is turned on with an inlet pressure that is above the recommended 1-70 mTorr, the foreline pressure may build and back up into the pump housing. Diffusion pumps can be safely used in the 100 mTorr range only if they are throttled, reducing the pressure at the inlet by limiting gas flow with smaller area before the inlet. When pressure goes up, the boiling point increases, and the higher temperatures break down the oil molecules causing them to be deposited as hydrocarbons on the surfaces of the diffusion pump.[29] The Diffusion Pumps were removed, cleaned, and refilled with 100 cubic centimeters of Kurt J. Lesker 704 silicone diffusion pump fluid.

### *3.2.5 Isolation and Bypass of Desiccator Leak*

The desiccator area was not holding sufficient vacuum (minimum  $4.0 \times 10^{-1}$  Torr). The hose to the desiccator was detached and capped off with a pressure gauge. The pressure now goes consistently down to a magnitude of  $10^{-2}$  Torr. It is possible that the seal around the door of the desiccator and/or the valve that isolates the desiccators may have leaks.

## *Chapter 4*

### CONCLUSION

#### **4.1 Summary**

The TEM, first invented in 1931, is a valuable tool for probing the nature of matter, especially for examining structure of materials and organisms on the nanometer scale. Using the high magnification and resolution capabilities of the TEM, the molecular and atomic morphology, composition, and crystallography of materials can be observed and studied. The proper functioning of the JEOL 100CX TEM at Houghton College depends on the cooperation of three main systems, the vacuum system, the electron gun, and the electromagnetic lens system used to manipulate and focus the electron beam.

The vacuum system of the TEM consists of rotary vane mechanical pumps to obtain rough vacuum and oil diffusion pumps to obtain the high vacuum conditions needed for the passage of the high-powered electron beam. A series of automated valves connect the various chambers to the pumps. The pressure in various chambers is monitored by pressure gauges connected to a computer system that monitors the pressure and controls the pumping process. The vacuum system was tested, analyzed, and modified to partial manual control for troubleshooting purposes.

At the conclusion of this research, both rotary vane pumps were functioning well, but the main column was not reaching sufficient rough vacuum pressure. The rotary vane pumps should be able to hold vacuum in the  $\sim 10^{-3}$  Torr range. If they cannot, that indicates a leak, contamination, or bad pumps. They only need to reach  $\sim 70 \times 10^{-3}$  Torr in order to switch to high vacuum with the oil diffusion pumps. The oil diffusion pumps were cleaned and the oil was changed.

Further research and testing by fellow student Justin Keeler determined that the main column could reach sufficient rough vacuum pressure to be pumped by the diffusion pumps, and that the diffusion pumps work well enough to reach pressures in the  $10^{-6}$  Torr range. The electron beam is functional, and an image can be projected and viewed on the phosphor screen.

## 4.2 Future Work

One of the hopes for this restoration project is for the JEOL 100CX TEM to be used in the study and characterization of thin metal films. An evaporation deposition chamber has been constructed, and plans and construction of a variable temperature Atomic Force Microscope (AFM) are under way. The TEM can be used to characterize the crystal structure of various thin metal films by producing diffraction patterns that can be analyzed in order to determine plane spacing and orientation of atomic layers.

Currently, the TEM does not interface directly with a computer, and does not produce digital images. Future work plans include connecting the PMT to a computer so that digital scan images can be produced and analyzed. The electron optics will need to be aligned and a sample prep lab needs to be developed in order for the capabilities of the 100CX to be applied to thin film research.

## Appendix A:

### Modified Systems

This appendix contains diagrams of any modifications made to the JEOL 100CX for reference use.

#### **A.1 Manual/Automatic Transfer Switch**

A caution relating to both the Manual/Automatic transfer switch and the previously used manual switch for valves 10, 25, and 26:

A series of automatic operations that is partly switched over to manual control may lead to damage because a valve is not opened or closed in the correct sequence. For example, if valves 10, 25, and 26 are manually opened to pump down the main column to rough vacuum pressure, and valves 7 and 8 open automatically because the pressure in the main column is low enough to now be pumped down to high vacuum by the diffusion pumps, they may open before valves 10, 25, and 26 are closed – leading to backstreaming contamination due to the pressure differential between the diffusion pumps and the rotary vane pumps. Therefore, the manual mode should only be used on a limited basis for isolating chamber sections and valves to search for leaks.

A test sampling of the wires returning to the system from the lower potential side of the solenoid valves showed that they were not all at ground potential. This is why the ‘automatic’ mode could not be wired so that all the low-potential wires were connected to a common ground.

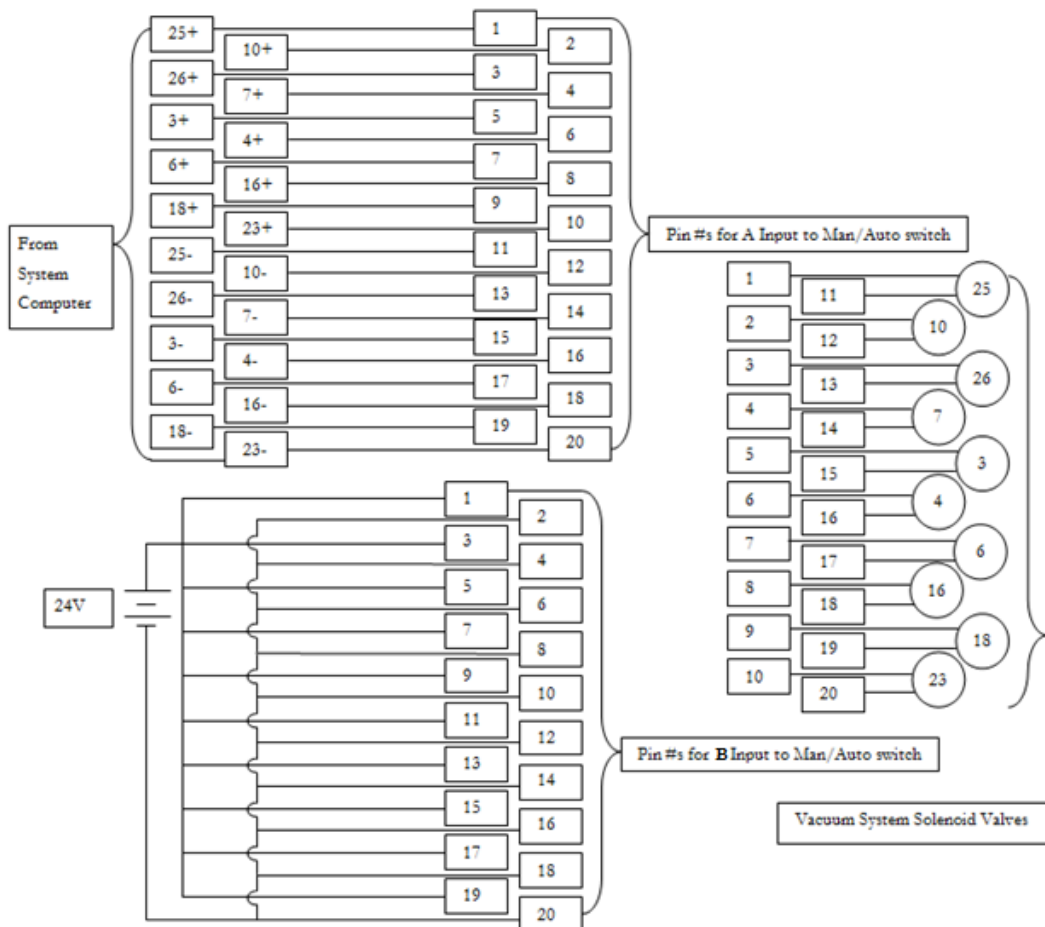


Figure 67 Diagram of the Auto/Manual Mode transfer switch. When the switch is in A (Automatic) mode, there are 10 circuits completed with a higher potential incoming line, a solenoid resistive load, and a lower potential outgoing line. In B (Manual) mode, there are 10 parallel solenoids connected to a 24V DC source and a common ground. The circuits of the 'off' mode once one is chosen to be 'on' are left open with no resistive load.

## A.2 Molecular Sieve

Pellets were baked in a vacuum oven for 37 hours at 170°C at a pressure of ~20 Torr with a slow bleed of inert Argon gas to purge the oven by momentum transfer as the oil molecules evaporated from the molecular sieve pellets. Because the pressure inside the oven was not precisely monitored, it is unclear whether this temperature and pressure combination was sufficient to vaporize the majority of the oil trapped in the molecular sieve pellets. The pump used during the bake is capable of attaining

pressures as low as  $2.1 \times 10^{-2}$  Torr, but the partial pressure of Argon gas was not monitored during the bake. The boiling point of the Welch Directorr Premium vacuum pump oil used in Rotary Pump 2 is 445°C. An estimate of the boiling point at different pressures can be made using the Trenton-Hildebrand-Everett rule.[32] In order to boil at 160-165°C, the pressure would have to be in the range of  $5.0 \times 10^{-1}$  Torr.

## Appendix B:

### Derivation for Relativistic Momentum of an Electron

The relation between total relativistic energy  $E$  and relativistic momentum  $p$  for a particle is

$$E^2 = p^2 c^2 + m_0^2 c^4 = p^2 c^2 + E_0^2. \quad (37)$$

This can be rearranged as

$$p^2 c^2 = E^2 - E_0^2. \quad (38)$$

Adding zero in the form of  $2EE_0 - 2EE_0$  and substituting  $-E_0^2 = E_0^2 - 2E_0^2$  results in

$$p^2 c^2 = E^2 + E_0^2 - 2E_0^2 + 2EE_0 - 2EE_0. \quad (39)$$

Regrouping,

$$p^2 c^2 = 2EE_0 - 2E_0^2 + (E^2 - 2EE_0 + E_0^2), \quad (40)$$

and factoring gives

$$p^2 c^2 = 2E_0(E - E_0) + (E - E_0)^2. \quad (41)$$

Change in relativistic kinetic energy  $\Delta E$  can be defined as

$$\Delta E = E - E_0. \quad (42)$$

Substituting using equation (6) and dividing by  $c^2$  gives

$$p^2 = \frac{2E_0 \Delta E}{c^2} + \frac{\Delta E^2}{c^2}. \quad (43)$$

Substituting  $E_0 = m_0 c^2$  gives momentum in terms of rest mass:

$$p^2 = 2m_0 \Delta E + \frac{\Delta E^2}{c^2}. \quad (44)$$

Finally, solving for  $p$  gives an expression for the momentum of a relativistic particle if the change in energy from rest is known:

$$p = \sqrt{2m_0\Delta E + \frac{\Delta E^2}{c^2}}. \quad (45)$$

## Appendix C:

### Specimen Holders

#### C.1 Common specimen holder

Table 2. Common specimen holder specifications.

Capacity	2 specimens
Tilt	single axis tilt
Applications	used with EM-BR bulk specimen retainer for secondary electron imaging
	graphite specimen retainer for use with STEM and x-ray analysis

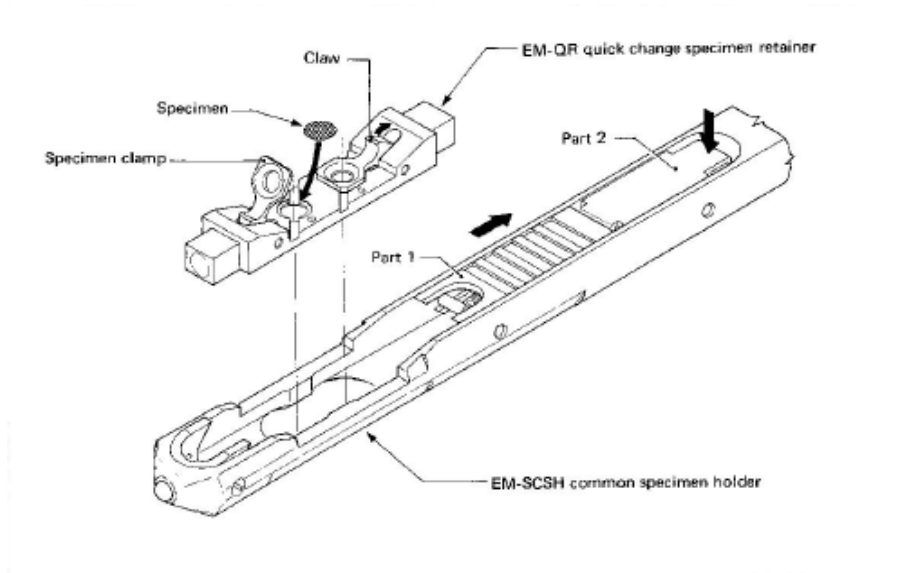


Figure 68. Common Specimen holder. Utilizes quick-exchange retainer and has spaces for two specimens.

## C.2 EM-BST Tilting specimen holder

Table 3. EM-BST tilting specimen holder specifications.

Capacity	2 specimens
Tilt	Adds y-axis tilt; $\pm 45^\circ$ ; speed $5^\circ - 50^\circ/\text{min}$
Applications	x- and y-tilt allow for all orientations within tilt range

When using both x- and y-tilt, the resultant tilt angle and azimuth can be found using the resultant angle and azimuth graph (Figure 69).

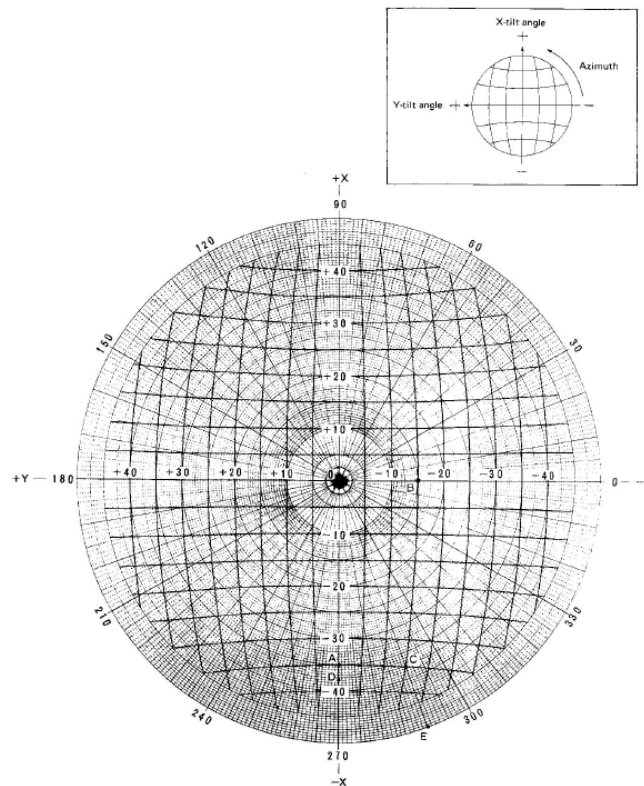


Figure 69. X-tilt and y-tilt azimuth graph. Taking the x-tilt angle from the SEG and the y-tilt angle from the tilting holder, the resultant tilt angle can be read from this graph. If the x-tilt angle is  $-35^\circ$  and the y-tilt angle is  $-15^\circ$ , then the resultant tilt angle is  $\sim 38^\circ$ , and the azimuth is approximately  $290^\circ$ . [25]

### C.3 BSR Rotating Holder

Table 4. BSR rotating holder specifications.

Capacity	1 specimen
Rotation	$\pm 360^\circ$ ; continuous
Applications	rotation and x-axis tilting allow for all orientations within x-axis tilt range

Appendix D:

Additional Diagrams and Schematics

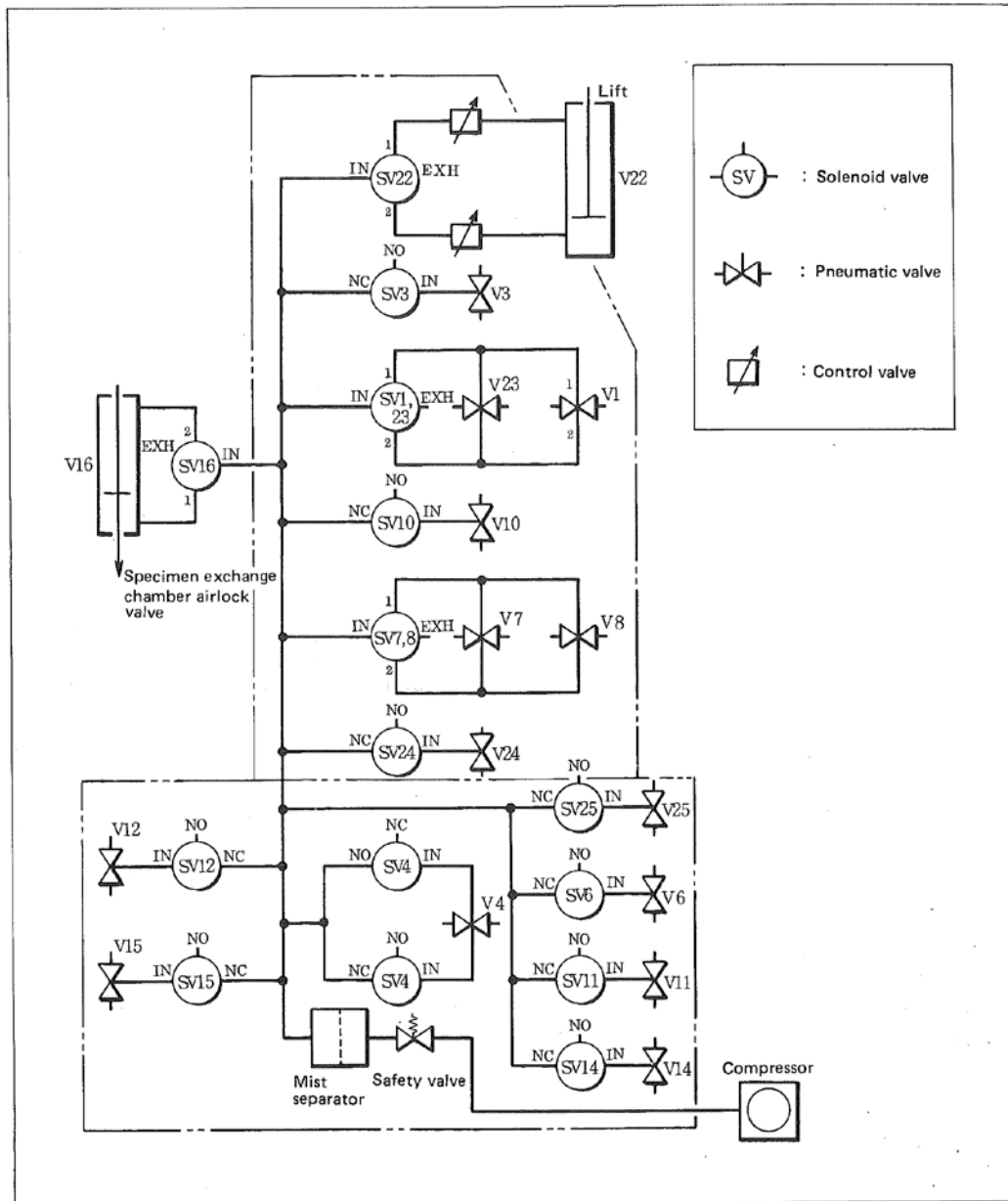


Figure 70. Compressed air system schematic showing how solenoid valves control air flow to open or close the vacuum system valves. Note that V7,V8 and V1,V23 are controlled by the same solenoid valve and operate simultaneously. The schematic also shows the specimen exchange chamber airlock and the lift mechanism used when the anode chamber is opened.

## References

---

- [1] D.B. Williams and C.B. Carter, *Transmission Electron Microscopy: A Textbook for Materials Science Basics I*. (Springer, New York, 1996).
- [2] L. de Broglie, *Comp. Rend.* **177**, 507 (1923).
- [3] E. Thomson, *Annu. Rep. Board Regents Smithson. Inst.* 239 (1914).
- [4] N. Bohr, *Philos. Mag.* **26**, 476 (1913).
- [5] L. DeBroglie, Ph.D. Thesis, University of Paris, (1924).
- [6] P.A. Tipler and R.A. Llewellyn, *Modern Physics*, (Macmillan, 2008).
- [7] C. Davisson and L.H. Germer, *Phys. Rev.*, **30**, 705 (1927).
- [8] G. P. Thomson, *Proc. R. Soc. A.* **117**, 600 (1928).
- [9] M. Knoll and E. Ruska, *Z. Physik* **78**, 318 (1932).
- [10] H. Busch, *Ann, Physik* **81**, 974 (1926).
- [11] M.M. Freundlich, *Sci. New Series*, **142**, 185 (1963).
- [12] E. Ruska, Ph.D. Thesis, Technischen Hochschule zu Berlin, (1933).
- [13] E.J. Big, *Bios.*, **27**, 33 (1956).
- [14] B.K. Vainshtein, *Structure Analysis by Electron Diffraction*, (Pergamon Press, Oxford 1964).
- [15] W.L. Bragg, *P. Camb. Phil. S.*, **17**, 43 (1913).
- [16] W. Friedrich, P. Knipping and M. Laue, *Ann. Phys.*, **346**, 971 (1913).
- [17] M. Vijayalakshmi *et al.*, *Sadhana*, **28**, 764 (2003).
- [18] D. Muller, "Introduction to Electron Microscopy" Cornell Center for Materials Research, Cornell, 2008 (unpublished).
- [19] Y. Lu and A. R. Barron, "Transmission electron microscopy: a module." <http://cnx.org/contents/7beccb58-2358-45e8-b274-c9cf40d36819@1>. (Viewed October 2013).
- [20] D. Alexander, EPFL (Lousanne, 2010).
- [21] P. Schroeder, University of Georgia, 2014 (unpublished).
- [22] G.S. Rohrer, *Structure and Bonding in Crystalline Materials* (Cambridge University Press. 2001).
- [23] L.A. Bendersky and F.W. Gayle, *J. Res. Natl. Inst. Stand. Technol.* **106**, 997 (2001).
- [24] R.F. Egerton, *Rep. Prog. Phys.*, **72**, 1 (2009).
- [25] JEOL Ltd, JEM-100CX Instructions (manual), (Tokyo).

- 
- [26] G. Moldovan, *et al.*, University of Oxford, 3 (Glasgow, 2008).
- [27] W.D. Reece and W.H. Hsu, Texas A&M University, Dept. Nuc. Eng., 34 (2013).
- [28] S.P. Hansen, *The Bell Jar*, **1** (1992).
- [29] V. Lindberg, *Chapter 6 Vacuum Pumps*, 8 (Roch. Inst. Tech., April 2008).
- [30] A. Berman, *Total Pressure Measurements in Vacuum Technology*, 140-2 (Academic Press, Inc., 1985).
- [31] F. Krumeich, Swiss Fed. Inst. of Tech. <http://www.microscopy.ethz.ch/se.htm> (viewed April 2014).
- [32] Everett, D. H. J. *Chem. Soc.* 1960, 2566–2573.